actuators

MDPI

Article

A Double-Integral Global Fast Terminal Sliding Mode Control with TD-LESO for Chattering Suppression and Precision Tracking of Fast Steering Mirrors

Xiaopeng Jia, Qingshan Chen *, Lishuang Liu and Runqiu Xia

School of Instrumentation Science and Optoelectronic Engineering, Beijing Information Science and Technology University, Beijing 100192, China; jxp2358278@163.com (X.J.); liulishuang@bistu.edu.cn (L.L.); xrq@bistu.edu.cn (R.X.)

* Correspondence: chenqqss@sina.com

Abstract

This paper describes a composite control approach that improves the accuracy and dynamic performance of the control of a voice-coil-driven, two-dimensional fast steering mirror (FSM). Strong nonlinearity, perturbation of parameters, unmodeled dynamics and external disturbances typically compromise the performance of the FSM. The proposed controller combines a tracking differentiator (TD), linear extended state observer (LESO), and a double-integral global fast terminal-sliding mode control (DIGFTSMC). The TD corrects the reference command signal, and the LESO approximates and counteracts system disturbances. The sliding surface is then equipped with the double-integral operators and an improved adaptive reaching law (IARL) to enhance tracking accuracy, response speed and robustness. Prior to physical experiments, systematic numerical simulations were conducted for five control algorithms across four typical test scenarios, verifying the proposed controller's feasibility and preliminary performance advantages. It is found through experimentation that the proposed controller lowers the time esterified by the step response adjustment by 81.0% and 48.4% more than the PID controller and the DIGFTSMC approach with no IARL, respectively, and the proposed controller enhances error control when tracking sinuoidal signals and multisinusoidal signals. Simulation results consistently align with experimental trends, confirming the proposed controller's superior convergence speed, tracking precision, and disturbance rejection capability. Furthermore, it cuts the angular movement swing by an average of over 44% through dismissing needless vibration interruptions as compared to other sliding mode control techniques. Experimental results demonstrate that the proposed composite control approach significantly enhances the disturbance rejection, control accuracy, and dynamic tracking performance of the voice-coil-driven FSM system.

Keywords: voice-coil motor fast steering mirror; double-integral sliding mode controller; parameter identification; tracking differentiator; linear extended state observer; control accuracy; disturbance rejection

Check for updates

Academic Editors: Oscar Barambones, Jose Antonio Cortajarena and Patxi Alkorta

Received: 26 November 2025
Revised: 28 December 2025
Accepted: 8 January 2026
Published: 10 January 2026

Copyright: © 2026 by the authors. Licensee MDPI, Basel, Switzerland. This article is an open access article distributed under the terms and conditions of the Creative Commons Attribution (CC BY) license.

1. Introduction

Fast steering mirrors (FSMs) comprise a precision optical actuator, which is known to respond quickly with a large control band and with high accuracy in tracking [1–6]. They are widely employed in high-bandwidth beam steering and fine tracking applications [7–10]. Although such benefits are provided, FSM systems experience violent

nonlinearities, changes in parameters, unmodeled dynamics, and internal and external disturbances. These may severely impair their tracking performance, both during large-deflection transients and under different operating conditions. Follow-up model variations due to temperature changes and the creep of materials only add more modeling uncertainty, which causes decreased robustness and control accuracy. In addition, nonlinearities are subject to external disturbances, so their presence can result in performance degradation and eventual instability.

To enhance the control performance of such systems, researchers have proposed a variety of control algorithms. Early studies generally adopted PID controllers, but their linear compensation was not effective in dealing with parameter perturbations and external disturbances, and was prone to causing overshoot and steady-state oscillations. Therefore, scholars have turned to more robust control strategies, such as sliding mode control (SMC), fuzzy PID control [11], model predictive control [12], H_∞ robust control [13], and active disturbance rejection control (ADRC) [14], etc. Among these methods, sliding mode control is widely used due to its strong robustness, fast response, and insensitivity to parameter perturbations and disturbances. However, traditional SMC faces challenges, such as chattering and slow convergence rates, particularly in systems with significant nonlinearities or varying parameters.

Several advanced sliding mode techniques have been developed to overcome these challenges. The SMC proposed in ref. [15] improves dynamic performance by suppressing chattering, but the linear sliding mode surface cannot ensure that it will reach equilibrium within a limited time. For this purpose, terminal sliding mode control (TSMC) [16] introduced terminal attractors to improve the convergence rate, but the fractional exponential term brought about the singularity problem. The non-singular terminal sliding mode control (NTSMC) [17] eliminates this problem and retains the characteristics of high precision and fast convergence. The non-singular fast terminal sliding mode control (NFTSMC) [18,19] further achieves finite-time stable control. However, its robustness is mainly reflected in the sliding mode stage, and it still has limitations in finite-time convergence. To ensure the robustness of the system, SMC usually requires a relatively large switching gain. However, an overly large gain will introduce high-frequency noise, while an overly small gain will cause the error to not converge. For this reason, refs. [20,21] proposed an adaptive mechanism to dynamically adjust the gain, but did not estimate the interference of unknown systems, resulting in a decrease in robustness.

Recent studies have applied RBFNN-based adaptive sliding mode control for trajectory tracking in uncertain systems with time-varying parameters [22]. RBFNN provide feedforward compensation by estimating uncertainties, while adaptive laws prevent excessive gains. However, approximation errors and parameter variations challenge sustained performance. Similarly, adaptive terminal sliding mode control uses nonlinear surfaces for finite-time convergence [23], with barrier functions estimating disturbances to ensure robustness. Yet, its complex tuning and design hinder practical use in highly uncertain environments. Furthermore, sliding mode observers are employed in descriptor systems requiring simultaneous state and unknown input estimation [24]. System reformulation to achieve infinite observability improves estimation and disturbance rejection, but implementation complexity remains a challenge for high-dimensional, real-time applications. In addition, LMI-based fuzzy observer–controllers integrate SMOs with Takagi–Sugeno models for uncertain MIMO systems [25], ensuring stability but suffering from computational complexity and inadequate real-time disturbance estimation for high-speed FSM applications.

A better global fast terminal sliding mode control (GFTSMC) is proposed to address the inherent nonlinear dynamics and external disturbances of FSM systems [26–28]. The innovation of the proposed method lies in combining a tracking differentiator (TD), the

linear extended state observer (LESO), the DIGFTSMC, and the improved adaptive reaching law (IARL). The TD smooths reference commands, reducing noise, while the LESO approximates lumped disturbances in real time, providing feedforward compensation. The DIGFTSMC, with double-integral terms, enhances convergence speed and reduces steady-state errors, which is essential for systems with rapid disturbances and uncertainties. Additionally, the integration of IARL optimizes convergence by adapting the system's control gains in real time, ensuring smooth error reduction and improved tracking accuracy.

Unlike traditional SMC approaches, which may require large switching gains and are prone to chattering, the proposed composite controller achieves robust disturbance rejection, high tracking accuracy, and fast convergence by effectively handling real-time disturbances and uncertainties. Moreover, the integration of IARL optimizes system performance, balancing rapid convergence and minimizing chattering, which is not adequately addressed in prior methods. Experimental results confirm that the proposed controller outperforms existing methods significantly: compared with the PID controller and the DIGFTSMC approach with only IARL, the step response settling time is reduced by 81.0% and 48.4%, respectively; in trajectory tracking tasks, the MAE and RMSE are decreased by 87–89% relative to the PID controller and 46–52% relative to the DIGFTSMC approach with only IARL; in random vibration disturbance rejection, the proposed controller reduces the MAX by over 44% compared to other sliding mode control approaches in three random vibration tests. The MAE is reduced by 37–41% relative to the DIGFTSMC approach with only IARL, and the RMSE remains below 8.7″, while other approaches exceed 13.8″.

The bottom part of the paper is structured as follows: Section 2 will give an analysis of the FSM system and its limitations, identifying the uncertainties that influence its performance. Section 3 presents the design of the proposed controller, emphasis being placed on the integration of TD, LESO, IARL, and DIGFTSMC. Section 4 is a discussion of the results of the simulation, which shows that the proposed controller is feasible. In Section 5, experimental verification is given, wherein the controller is verified to work on an actual FSM. Lastly, Section 6 wraps up the paper by highlighting the findings of this research and indicating possible directions for future studies.

2. Analysis of Constraints and Uncertainties in FSM System Performance

The FSM system has several constraints and uncertainties that limit its performance. These have great implications for its efficiency and reliability. These limitations are important to understand to make the system perform in an optimal way. To begin with, the design limitations of the FSM system are very difficult to overcome. They include software incompatibilities and hardware restrictions, which may hinder performance. As an example, a time constraint in processing power may hamper the system's capacity to perform complicated tasks effectively. Additionally, there are environmental factors that produce uncertainties and can thus cause variation in the functioning of the FSM system. Changes in temperature and humidity and electromagnetic disturbances may cause unpredictable performance results. These environmental factors require effective design solutions so as to counter their effects. Also, some differences in performance are based on user-related factors. The situational differences in users' levels of experience and interactional patterns may lead to an ineffective use of the system as a whole. To deal with such problems, training and improvement of the user interface are required. To conclude, the performance of the FSM system is limited by its design constraints, uncertainties in the environment, and other factors pertaining to users. Those are challenges that have to be addressed with specific strategies that would improve the efficiency and reliability of these systems.

The proposed voice coil motor FSM will consist of a mirror, bracket, base, voice coil motor, eddy current displacement sensor, flexible support structure, and the main controller module. The support structure is flexible and employs elastic components for accurate swinging. The sensor that measures the angle of rotation takes readings on the position of the mirror. The primary controller module uses sensor readings and control inputs. The voice coil motor gives the required torque for the swift response and proper angle adjustment. The structure of the FSM system is shown in Figure 1.

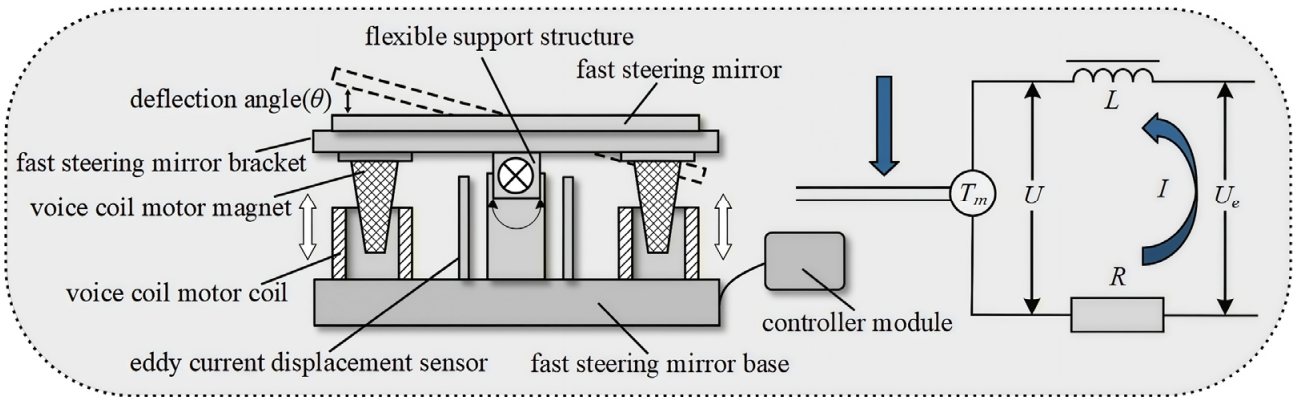


Figure 1. Structural design of the FSM system.

The voice coil motor generates electromagnetic force using a non-contact push–pull method, which applies torque to rotate the load mirror. Its mathematical model is depicted in Figure 2. In this model, s represents the complex frequency domain variable post-Laplace transform. The input voltage is denoted by $U(s)$, and the FSM's deflection angle is $\theta(s)$. Inductance and resistance of the coil circuit are represented by L and R, respectively, while I denotes the coil current. The moment of inertia is indicated by J_m. The total viscous damping coefficient is B_m, and the elastic coefficient of the flexible hinge is K_s. The electromagnetic torque constant is K_t, and the back electromotive force coefficient is K_e. The physical parameters involved in the FSM model, together with their units and physical meanings, are summarized in Table 1.

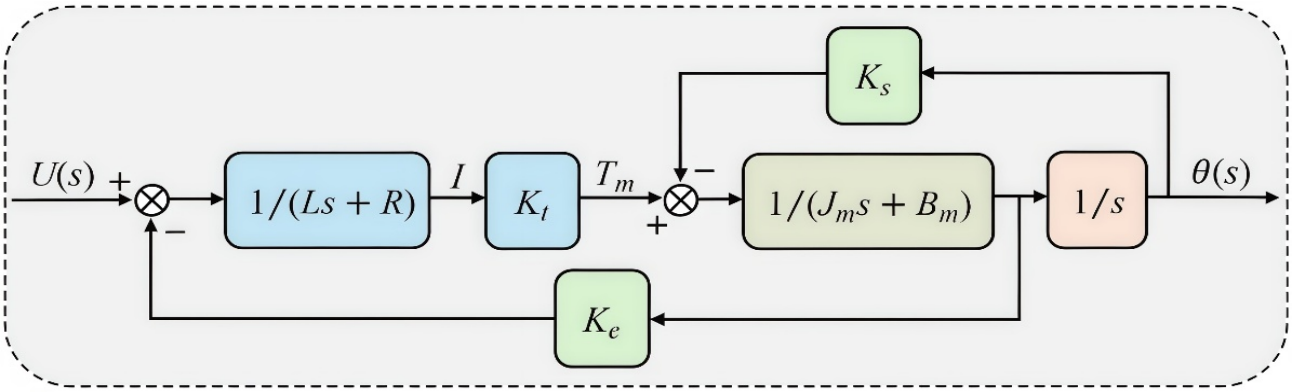


Figure 2. Mathematical model of voice coil actuator fast steering mirror.

Table 1. Physical model parameters of the FSM system.

Physical Parameter	Unit	Physical Significance
R	Ω	resistance
L	H	inductance
K_e	V·s/rad	back electromotive force constant
I	A	current
J_m	Kg·mm^2	moment of inertia
K_t	Nm/A	electromagnetic torque constant
K_s	N/m	hinge elastic coefficient
B_m	N·s/m	damping coefficient
U	V	input voltage
U_e	V	back electromotive force

The circuit balance and torque balance equations for the voice coil motor are presented below:

$$U = RI + L\frac{dI}{dt} + K_e\frac{d\theta}{dt} \tag{1}$$

$$T_m = J_m\frac{d^2\theta}{dt^2} + B_m\frac{d\theta}{dt} + K_s\theta \tag{2}$$

where Equation (1) shows the motor converting electrical to mechanical energy, opposing the back electromotive force. Equation (2) models the system's dynamics, with inertia governing response speed, and damping and elasticity influencing stability and oscillations.

The output torque of the voice coil motor is represented by $T_m = K_t \cdot I$, while the back electromotive force is denoted by $U_e = K_e \cdot d\theta/dt$. The core value, quantifying the electromechanical coupling, is reflected in the FSM system's transfer function, derived through formula integration and Laplace transform.

$$G(s) = \frac{\theta(s)}{U(s)} = \frac{K_t}{LJ_ms^3 + (LB_m + RJ_m)s^2 + (RB_m + K_tK_e + LK_s)s + RK_s} \tag{3}$$

Given the relatively small inductance of parameter L, its effect on the mathematical model can be disregarded. Consequently, the transfer function model of the voice coil motor FSM system is simplified to:

$$G(s) = \frac{\theta(s)}{U(s)} = \frac{G_0}{s^2 + P_0s + Q_0} \tag{4}$$

where $P_0 = \frac{K_s}{J_m}$, $Q_0 = \frac{RB_m + K_tK_e}{RJ_m}$, and $G_0 = \frac{K_t}{RJ_m}$.

This section establishes the second-order FSM system transfer function model, as depicted in Equation (4), through mechanism modeling. The equivalent damping ratio ζ ($\zeta \propto Q_0$) and undamped natural frequency ω_n ($\omega_n \propto \sqrt{P_0 + G_0Q_0}$), determined by nominal physical parameters (J_m, B_m, K_s, etc.), inherently restrict the system's dynamic response speed and stability accuracy. In addition, parameter perturbations, unmodelled dynamics, and external disruptions in operation enhance the ambiguity of the dynamic nature of the system. This uncertainty, therefore, goes a long way to compromise the operating characteristics of classical controllers based on the nominal model.

To establish a clear foundation for the subsequent control design and analysis, key prerequisites, constraints, and simplifications inherent to the voice-coil-driven FSM system are summarized in Table 2. They are derived from the system's mechanical–

electromagnetic characteristics, practical hardware constraints, and engineering implementation feasibility, ensuring the proposed control approach is both theoretically rigorous and practically applicable.

Table 2. List of physical assumptions, actuator limits, uncertainties, and model simplifications.

Category	Specific Details
physical assumptions	Lumped disturbances (nonlinearities, parameter perturbations, external vibrations) are bounded with negligible derivatives
actuator limits	Angular deflection: ±26.2 mrad (constrained by flexible hinge mechanical stroke); Voice coil motor drive current/voltage comply with rated parameters (thermal overload prevention); Angular velocity/acceleration limited by voice coil motor thrust and structural strength
uncertainties	Parameter drift (temperature variation, material creep); unmodeled high-frequency dynamics; Eddy current sensor measurement noise; Random external vibration disturbances
model simplifications	Coil inductance (L) is neglected; FSM approximated as a second-order transfer function model

3. Controller Design and Analysis

To overcome the challenges mentioned above, the current paper recommends the abandonment of old-school approaches that rely on exact models. Rather, it proposes a solid control strategy focused on disturbance observation and compensation. This strategy employs TD to filter the reference command, hence decreasing noise. It uses LESO to predict system disturbances in real-time and implement feed-forward compensation. Also, the closed-loop law of control of the FSM system is generated with the help of DIGFTSMC. Figure 3 shows the block diagram of the proposed controller.

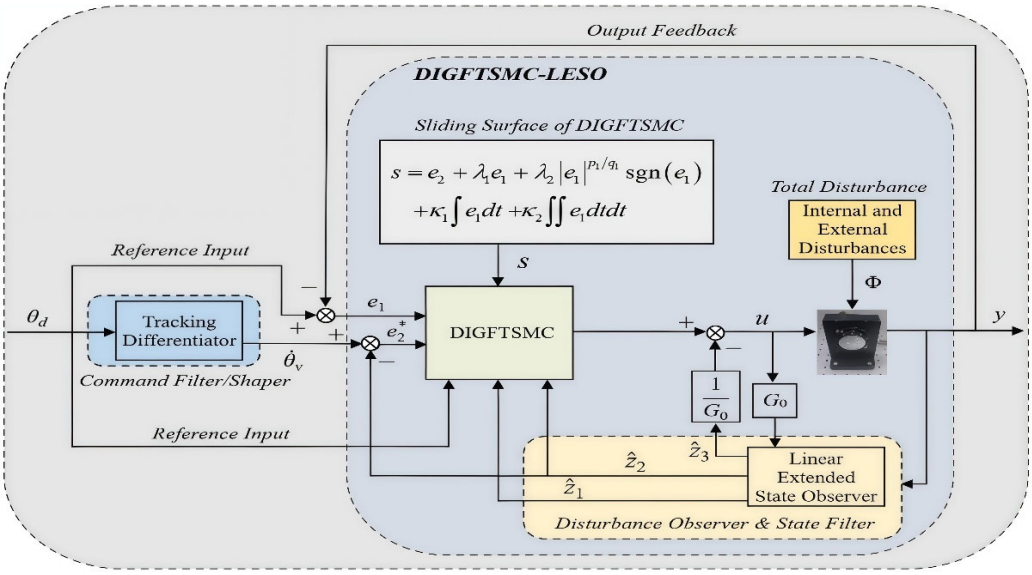


Figure 3. Block diagram of the TD-DIGFTSMC-LESO controller.

3.1. Tracking Differentiator

As a front-end signal processing module, TD effectively generates a smooth reference trajectory and differential signals. It dynamically plans the transient process of the input

signal to balance rapid response with overshoot suppression. The discrete form equation is structured as follows:

$$\begin{cases} \theta_v(k+1) = \theta_v(k) + T\dot{\theta}_v(k) \\ \dot{\theta}_v(k+1) = \dot{\theta}_v(k) + T\ fhan\Big(\theta_v(k) - \theta_d(k), \dot{\theta}_v(k), r_0, h_0\Big) \end{cases} \tag{5}$$

The reference input signal is denoted by θ_d. The TD tracking signal and its differential value are represented by θ_v and $\dot{\theta}_v$ respectively. The sampling period is indicated by T. The fast factor is r_0, while the filtering factor is h_0. Lastly, the fast optimal control synthesis function is denoted by $fhan(\cdot)$ [29].

3.2. Linear Extended State Observer

LESO deals with strong nonlinearities, changes in parameters, and unmodeled dynamics, as well as disturbances, by estimating these effects and equalizing them as a total disturbance via the extended state approach. In contrast to the conventional ESO, LESO boosts the efficiency of observation and real-time performance without lessening its strength. Its simplicity and the control of its parameters make it effective in high-precision servo controls. LESO is able to enhance the accuracy and durability of FSMs in cases with intricate disturbances.

In the context of the actual FSM system, consider a bounded, uncertain lumped disturbance, denoted by Φ. Assume there exists a constant $\Phi_\zeta \in \mathbb{R}^+$ such that $|\Phi| \leq \Phi_\xi$. Here, Φ_ξ represents the maximum amplitude of Φ. Referring to the complex frequency domain function model in Equation (4), the corresponding time-domain differential equation can be expressed as follows:

$$\ddot{y}(t) + Q_0\dot{y}(t) + P_0 y(t) = G_0 u(t) + \Phi(t) \tag{6}$$

Let $x_1 = y(t), x_2 = \dot{y}(t)$. From Equation (6), the state-space equation of the FSM system is as follows:

$$\begin{cases} \dot{x}_1 = x_2 \\ \dot{x}_2 = -P_0 x_1 - Q_0 x_2 + G_0 u + \Phi(t) \\ y = x_1 + \Phi_v(t) \end{cases} \tag{7}$$

where x_1 and x_2 denote the system position and velocity states, respectively. u represents the control input, and y is the position output. Φ_v denotes the measurement noise introduced within the eddy current sensor, which arises due to inherent limitations in the sensor's precision and environmental factors that may affect the accuracy of the readings.

Based on Equation (7), the lumped disturbance of the FSM system Φ is introduced and represented as an extended state variable x_3. Consequently, Equation (7) is rewritten as follows:

$$\begin{cases} \dot{x}_1 = x_2 \\ \dot{x}_2 = x_3 - P_0 x_1 - Q_0 x_2 + G_0 u \\ \dot{x}_3 = \ \Phi(t) \end{cases} \tag{8}$$

This representation enables the construction of the following form of LESO:

$$\begin{cases} e_\theta = y - \hat{Z}_1 \\ \dot{\hat{Z}}_1 = \hat{Z}_2 + \beta_1 e_\theta \\ \dot{\hat{Z}}_2 = \hat{Z}_3 - P_0\hat{Z}_1 - Q_0\hat{Z}_2 + \beta_2 e_\theta + G_0 u \\ \dot{\hat{Z}}_3 = \beta_3 e_\theta \end{cases} \tag{9}$$

where e_θ denotes the deviation between the FSM position feedback and its estimated value. $\hat{Z}_i$ ($i = 1, 2, 3$) denote the estimated values of the FSM position angle, angular velocity, and the lumped disturbance of the system Φ. G_0 is the nominal value of the control gain, and β_i ($i = 1,\ 2,\ 3$) are the error feedback gains of each order of the LESO. The schematic of the third-order LESO is shown in Figure 4.

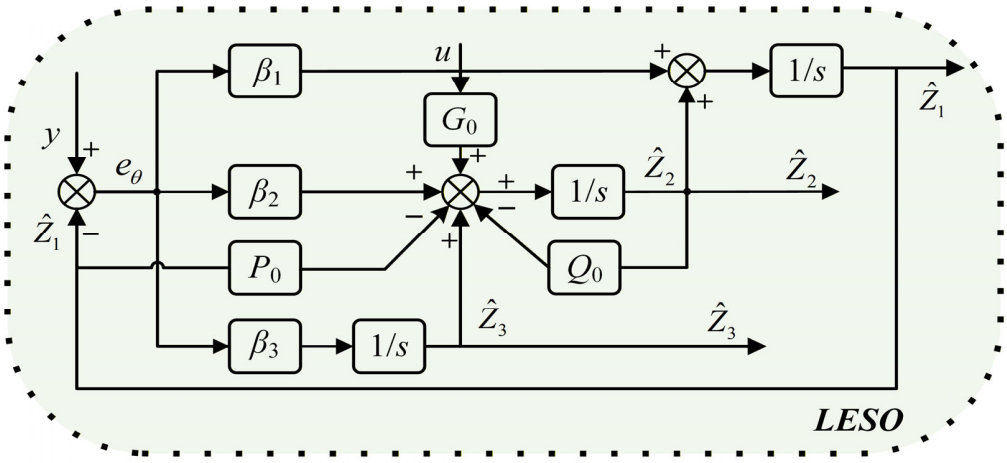


Figure 4. Schematic diagram of the third-order LESO.

As shown in Figure 4, the proposed model-assisted LESO design strategy separates the system's prior dynamic characteristics from the generalized disturbances and embeds them as feedforward information within the observer architecture. This allows error disturbances to be exactly estimated and compensated against in real time, decreasing, to a great extent, the estimation load on the observer. As compared to the conventional ESO, which is limited by its use of model information, this strategy uses model parameters that are acquired by means of system identification, making it much better in terms of disturbance rejection and dynamic performance.

The observation error of the LESO can be written as the following state-space equation:

$$\dot{\hat{\boldsymbol{e}}}_{\boldsymbol{LESO}} = \bar{\boldsymbol{A}}\hat{\boldsymbol{e}}_{\boldsymbol{LESO}} + \bar{\boldsymbol{B}}\dot{\Phi} = \begin{bmatrix} \dot{\hat{e}}_\theta \\ \dot{\hat{e}}_{\dot{\theta}} \\ \dot{\hat{e}}_\Phi \end{bmatrix} = \begin{bmatrix} -\beta_1 & 1 & 0 \\ -\beta_2 & 0 & 1 \\ -\beta_3 & 0 & 0 \end{bmatrix} \begin{bmatrix} \hat{e}_\theta \\ \hat{e}_{\dot{\theta}} \\ \hat{e}_\Phi \end{bmatrix} + \begin{bmatrix} 0 \\ 0 \\ 1 \end{bmatrix} \dot{\Phi} \tag{10}$$

where $\dot{\hat{e}}_{LESO} = \begin{bmatrix} \hat{e}_\theta \\ \hat{e}_{\dot{\theta}} \\ \hat{e}_\Phi \end{bmatrix} = \begin{bmatrix} \hat{Z}_1 - y \\ \hat{Z}_2 - \dot{y} \\ \hat{Z}_3 - \Phi \end{bmatrix}$, $\bar{\boldsymbol{A}} = \begin{bmatrix} -\beta_1 & 1 & 0 \\ -\beta_2 & 0 & 1 \\ -\beta_3 & 0 & 0 \end{bmatrix}$, $\bar{\boldsymbol{B}} = \begin{bmatrix} 0 \\ 0 \\ 1 \end{bmatrix}$. e_θ denote the position measurement error, $e_{\dot{\theta}}$ denotes the angular velocity measurement error, and e_Φ denotes the observed error of the system lumped disturbance. This equation describes the dynamic evolution of errors, providing a basis for tuning observer gains β_1, β_2, and β_3 to ensure asymptotic convergence of observation error, crucial for reliable state feedback control and disturbance compensation.

Given that $\dot{\Phi} \approx 0$ and its norm is upper-bounded $W > 0$, Equation (10) can be simplified to the homogeneous state equation $\dot{\hat{e}}_{\boldsymbol{LESO}} = \bar{\boldsymbol{A}}\hat{e}_{\boldsymbol{LESO}}$. The characteristic equation of $\bar{\boldsymbol{A}}$ is derived as follows:

$$f(\lambda) = \det\left(\lambda \boldsymbol{I} - \bar{\boldsymbol{A}}\right) = \lambda^3 + \beta_1\lambda^2 + \beta_2\lambda + \beta_3 = 0 \tag{11}$$

To minimize design parameters and enhance transient performance, the closed-loop characteristic equation of the LESO is defined as:

$$\chi_e(\lambda) = (\lambda + \omega_0)^3 = \lambda^3 + 3\omega_0\lambda^2 + 3\omega_0^2\lambda + \omega_0^3 \tag{12}$$

where ω_0 denotes the observer bandwidth parameter with $\omega_0 > 0$. According to [30], β_1, β_2, and β_3 can be expressed as:

$$\beta_1 = 3\omega_0, \qquad \beta_2 = 3\omega_0^2, \qquad \beta_3 = \omega_0^3 \tag{13}$$

To ensure the observer error converges asymptotically, parameters β_1, β_2, and β_3 are configured so that matrix $\overline{A}$ meets Hurwitz stability criteria. The observer gain, derived from Equation [13], is uniquely determined by parameter ω_0. This reduces tuning parameters, simplifying engineering implementation and debugging.

3.3. Design of Double-Integral Sliding Mode Terms

The proposed controller incorporates a double-integral strategy that puts double-integral terms onto a sliding surface, thus effectively doing away with steady-state errors. This is a very important strategy that can be used to improve the steady-state and transient performance of the system. With these functionality attributes, the closed-loop system is robust in performance with fast convergence, the chattering is alleviated, and the singularity problems are minimized. The sections that follow will describe the process of its design in detail.

To ensure precise tracking within the FSM system, the tracking position error function is defined as follows:

$$\begin{cases} e_1 = \theta_d - y \\ e_2 = \dot{\theta}_d - \dot{y} \\ \dot{e}_2 = \ddot{\theta}_d - \ddot{y} \end{cases} \tag{14}$$

where θ_d denotes the reference position signal, and e_1, e_2, $\dot{e}_2$ represent the angular error, angular velocity error, and the derivative of the angular velocity error of the FSM, respectively. These errors indicate tracking performance: minimizing e_1 ensures accuracy, while minimizing e_2 and $\dot{e}_2$ ensures smooth dynamics, allowing the controller to target the FSM's key metrics.

Using the tracking error from Equation (14), we can construct the first and second integral terms as follows:

$$\begin{cases} I_1 = \kappa_1 \int e_1 dt \\ I_2 = \kappa_2 \iint e_1 dt dt \end{cases} \tag{15}$$

The system's asymptotic stability ensures its state trajectory will converge to the sliding mode surface and approach the origin, where $s = 0$ and $\dot{s} = 0$. The gain coefficients, κ_1 and κ_2, which are associated with the integral terms I_1 and I_2, significantly influence the closed-loop system's dynamic response.

3.4. Design of TD-DIGFTSMC-LESO Controller

The conventional design of the GFTSMC sliding surface is outlined as follows:

$$s = e_2 + \lambda_1 e_1 + \lambda_2 |e_1|^{p_1/q_1} \mathrm{sgn}(e_1) \tag{16}$$

DIGFTSMC improves the sliding surface with the introduction of a double-integral operator. This innovation keeps the convergence swift and heading towards non-singularities and does not slow down the pace of error correction and convergence. It enhances the tracking performance of the systems in the presence of disturbances and uncertainties.

DIGFTSMC has significant advantages over traditional structures in its reduction in steady-state error, chattering minimization, and enhancement in accuracy. The sliding surface is arranged in the following way:

$$s = e_2 + \lambda_1 e_1 + \lambda_2 |e_1|^{p_1/q_1} \mathrm{sgn}(e_1) + \kappa_1 \int e_1 dt + \kappa_2 \iint e_1 dt dt \tag{17}$$

where λ_1, λ_2, κ_1, and $\kappa_2 > 0$, p_1 and q_1 are positive odd integers, with $0 < p_1/q_1 < 1$. The function $\mathrm{sgn}(\cdot)$ is the sign function.

By differentiating the sliding surface of the DIGFTSMC as presented in Equation (17) and integrating it with Equations (8) and (14), the following result is derived:

$$\dot{s} = \ddot{\theta}_d + P_0 x_1 + Q_0 x_2 - x_3 - G_0 u + \lambda_1 e_2 + \lambda_2 \frac{p_1}{q_1} |e_1|^{\frac{p_1}{q_1}-1} \mathrm{sgn}(e_1) e_2 + \kappa_1 e_1 + \kappa_2 \int e_1 d\, t \tag{18}$$

where this equation connects the sliding surface to the system's dynamics and disturbances, forming the basis for designing the reaching law to ensure finite-time convergence despite disturbances.

Directly measuring the reference input angular velocity $\dot{\theta}_d$ of the system and the angular velocity of the system feedback $\dot{y}$ tends to be difficult in real-world control systems. To eliminate this, the error between the desired angular velocity calculated by the TD and the estimated system output angular velocity calculated by the LESO, which is a dynamic error, is utilized to overcome it. This methodology allows for great accuracy in estimating the differential signal. This has the consequence that the angular error of velocity is redefined as e_2^*:

$$e_2^* = \dot{\theta}_v - \hat{Z}_2 \tag{19}$$

In choosing reaching laws, the GFTSMC typically employs the continuous reaching law (CRL), expressed as follows:

$$\dot{s} = -k_c s - \varepsilon_c s^{\frac{p_0}{q_0}} \tag{20}$$

where $k_c > 0$ and $\varepsilon_c > 0$. p_0 and q_0 are positive odd integers, with $0 < p_0/q_0 < 1$.

Equation (20) illustrates how the CRL substitutes the discontinuous switching term s^{p_0/q_0} with a continuous fractional power term $\mathrm{sgn}(s)$. This replacement helps counter the chattering phenomenon sufficiently. However, the predetermined gain of the CRL presents the dilemma of balancing the system's dynamic response and robust performance. To solve this, an improved adaptive reaching law (IARL) is presented. The IARL enables the gain to vary depending on the state of the system, improving both the dynamic response and steady-state performance of the FSM system. IARL can be explained as follows:

$$\begin{cases} \dot{s} = -f(e_1, s)\tanh(s) - k_2 g(s) s \\ f(e_1, s) = \varepsilon |e_1| / \left[k_1 + (1 - k_1) e^{-\vartheta |s|}\right] \\ g(s) = \beta \tanh(|s|) + \phi / [1 + \ln(1 + \varphi |s|)] \end{cases} \tag{21}$$

where ε, ϑ, k_1, k_2, β, ϕ, and φ are constants, with $\varepsilon > 0$, $\vartheta > 0$, $0 < k_1 < 1$, $k_2 > 0$, $\beta > 0$, $0 < \phi < 1$, and $\varphi > 0$.

By integrating Equations (18), (19), and (21) simultaneously, the DIGFTSMC law based on IARL is obtained as follows

$$\tau_{DIGFTSMC} = \frac{1}{G_0}\left\{\begin{array}{l} \ddot{\theta}_d + P_0 x_1 + Q_0 x_2 - x_3 + \lambda_1 e_2^* + \lambda_2 \frac{p_1}{q_1}|e_1|^{\frac{p_1}{q_1}-1}\mathrm{sgn}(e_1)e_2^* + \kappa_1 e_1 + \kappa_2 \int e_1 dt \\ + \frac{\varepsilon|e_1|}{k_1 + (1-k_1)e^{-\vartheta|s|}}\tanh(s) + k_2\left[\beta\tanh(|s|) + \frac{\phi}{1+\ln(1+\varphi|s|)}\right]s \end{array}\right\} \quad (22)$$

where this control law consists of two parts: the equivalent control term (derived from the zero-velocity condition of the sliding surface, $\dot{s} = 0$), ensuring dynamic performance on the sliding surface, and the switching control term (derived from the IARL), providing robustness against disturbances and parameter perturbations.

Given that the system state variables x_2 and lumped disturbances Φ are challenging to measure directly, to enhance state estimation accuracy and system robustness, Equation (23) is reconstructed through the LESO. Subsequently, the observer estimates $\hat{Z}_1$, $\hat{Z}_2$, and $\hat{Z}_3$ are used to replace the original system state variables x_1, x_2, and x_3, respectively, resulting in the final control law for driving the FSM system, as follows:

$$u = \frac{1}{G_0}\left\{\begin{array}{l} \ddot{\theta}_d + P_0 \hat{Z}_1 + Q_0 \hat{Z}_2 - \hat{Z}_3 + \lambda_1 e_2^* + \lambda_2 \frac{p_1}{q_1}|e_1|^{\frac{p_1}{q_1}-1}\mathrm{sgn}(e_1)e_2^* + \kappa_1 e_1 + \kappa_2 \int e_1 dt \\ + \frac{\varepsilon|e_1|}{k_1 + (1-k_1)e^{-\vartheta|s|}}\tanh(s) + k_2\left[\beta\tanh(|s|) + \frac{\phi}{1+\ln(1+\varphi|s|)}\right]s \end{array}\right\} \quad (23)$$

Figure 5 clearly illustrates the system implementation architecture of the control law u outlined in Equation (23). It details the signal transmission path and the closed-loop control mechanism between modules.

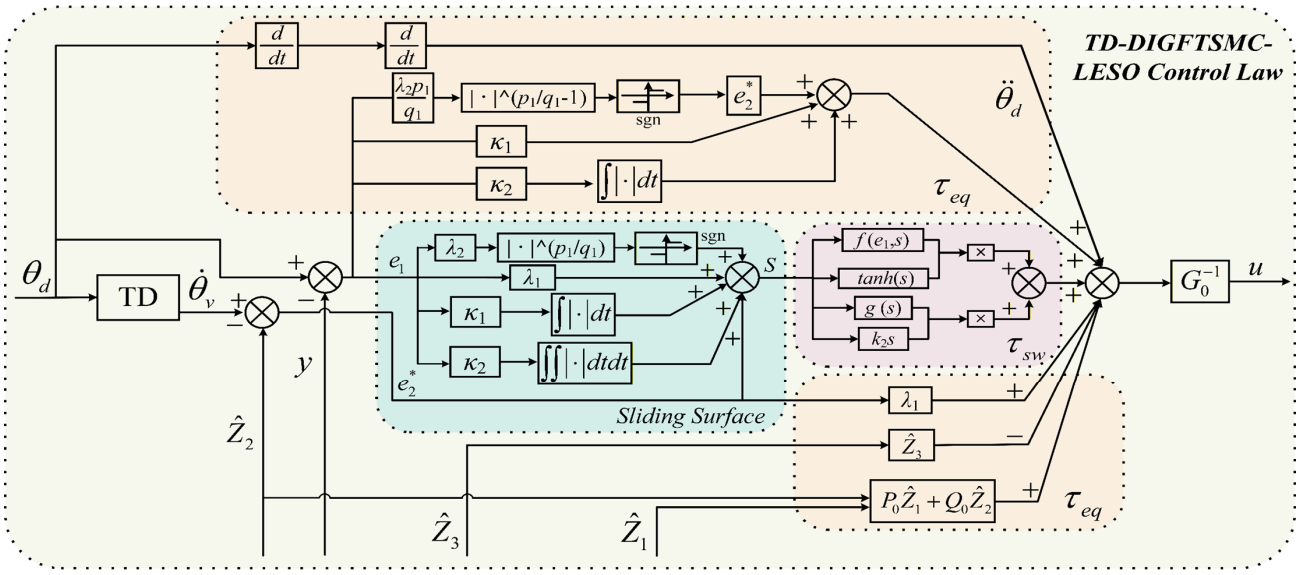


Figure 5. Block diagram of the TD-DIGFTSMC-LESO control law.

It is noteworthy that in the equivalent control law of Equation (23), the parameters β_1, β_2, and β_3 influence the convergence behavior of the state estimation variables $\hat{Z}_1$, $\hat{Z}_2$, and $\hat{Z}_3$. Increasing the characteristic frequency ω_0 accelerates the transient process of the observation error $\hat{\boldsymbol{e}}_{\boldsymbol{LESO}}$ approaching zero. Nevertheless, it should be remembered that there is a limit to the maximum value of ω_0 that should not be exceeded to prevent instability in the system. The switching control law has an adaptive control that dynamically adjusts the control gains. An expansion in the ε increases the magnitude of switching and can cause severe chattering. The parameter k_2 controls how quickly the system state reaches

the sliding surface. The added adaptive functionality ensures bounded gain, making the closed-loop system operate in a stable manner.

3.5. Superiority Analysis of the Improved Adaptive Reaching Law

In the MATLAB (R2023b) simulation, using the state-space model in Equation (8) and excluding the lumped disturbance Φ, various reaching laws are introduced: constant velocity $\dot{s} = -\varepsilon \mathrm{sgn}s$, exponential $\dot{s} = -\varepsilon \mathrm{sgn}s - ks$, power $\dot{s} = -k|s|^{\alpha}\mathrm{sgn}s$, the continuous reaching law in Equation (20), and the IARL in Equation (21). These are used to compare the dynamic responses and convergence performances of different reaching strategies. The parameters are set as $P_0 = 0$, $Q_0 = 25$, and $G_0 = 150$, with the reference input defined as $\theta_d(t) = \sin(t)$. The design of these reaching laws results in the sliding mode phase trajectories shown in Figure 6.

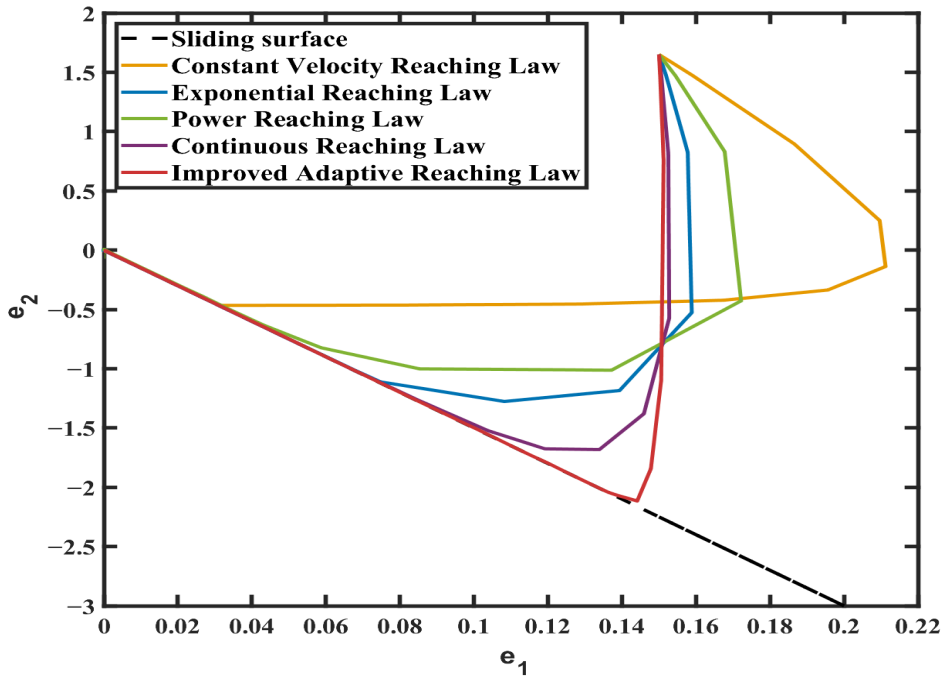


Figure 6. Phase trajectory of sliding mode motion.

Phase trajectory analysis demonstrates that the proposed IARL excels in both convergence speed and steady-state maintenance. Unlike other strategies, IARL swiftly and precisely guides the system state to the sliding mode surface, showcasing its superiority in dynamic quality enhancement and robustness. During various motion stages, IARL exhibits the following characteristics:

(1) When distanced from the sliding surface (i.e., $|s| \gg 0$), IARL induces a damping approach motion through the coupling effect of the nonlinear gain $f(e_1, s)$ and $\tanh(s)$. Specifically, $f(e_1, s) \approx \varepsilon|e_1|/k_1$ and $\tanh(s) \approx \mathrm{sgn}(s)$, which results in a rapid approaching term of $-\varepsilon|e_1|\mathrm{sgn}(s)/k_1$. At the same time, $g(s) \approx \beta$ provides linear damping of $-k_2\beta s$. This combination ensures a high dynamic response with fast tracking and effectively suppresses chattering.

(2) When approaching the sliding mode surface (i.e., $|s| \approx 0$), IARL demonstrates smooth convergence. The term $f(e_1, s)\tanh(s)$ degenerates into a quasi-sliding mode term of $-\varepsilon|e_1|s$, while the nonlinear structure of $g(s)$, given by $\phi/[1 + \ln(1 + \varphi|s|)]$, dominates in generating a control torque that asymptotically approaches zero. This mechanism reduces chattering and ensures asymptotic stability.

3.6. Stability Analysis of TD-DIGFTSMC-LESO

For any symmetric positive definite matrix Ω, there exists another symmetric positive definite matrix Θ that satisfies the Lyapunov equation:

$$\bar{\boldsymbol{A}}^{-\mathrm{T}}\Theta + \Theta\bar{\boldsymbol{A}} + \Omega = 0 \tag{24}$$

For the LESO, the following Lyapunov function is constructed to analyze its stability:

$$V_0 = \hat{\boldsymbol{e}}_{\boldsymbol{LESO}}^{\mathrm{T}}\Theta\hat{\boldsymbol{e}}_{\boldsymbol{LESO}} \tag{25}$$

By integrating Equation (10) and differentiating with respect to V_0, the following result is derived:

$$\begin{aligned}
\dot{V}_0 &= \dot{\hat{\boldsymbol{e}}}_{\boldsymbol{LESO}}^{\mathrm{T}}\Theta\hat{\boldsymbol{e}}_{\boldsymbol{LESO}} + \hat{\boldsymbol{e}}_{\boldsymbol{LESO}}^{\mathrm{T}}\Theta\dot{\hat{\boldsymbol{e}}}_{\boldsymbol{LESO}} \\
&= \left(\bar{\boldsymbol{A}}\hat{\boldsymbol{e}}_{\boldsymbol{LESO}} + \bar{\boldsymbol{B}}\dot{\Phi}\right)^{\mathrm{T}}\Theta\hat{\boldsymbol{e}}_{\boldsymbol{LESO}} + \hat{\boldsymbol{e}}_{\boldsymbol{LESO}}^{\mathrm{T}}\Theta\left(\bar{\boldsymbol{A}}\hat{\boldsymbol{e}}_{\boldsymbol{LESO}} + \bar{\boldsymbol{B}}\dot{\Phi}\right) \\
&= \hat{\boldsymbol{e}}_{\boldsymbol{LESO}}^{\mathrm{T}}\left(\bar{\boldsymbol{A}}^{-\mathrm{T}}\Theta + \Theta\bar{\boldsymbol{A}}\right)\hat{\boldsymbol{e}}_{\boldsymbol{LESO}} + 2\hat{\boldsymbol{e}}_{\boldsymbol{LESO}}^{\mathrm{T}}\Theta\bar{\boldsymbol{B}}\dot{\Phi} \\
&\le -\hat{\boldsymbol{e}}_{\boldsymbol{LESO}}^{\mathrm{T}}\Omega\hat{\boldsymbol{e}}_{\boldsymbol{LESO}} + 2\left\|\Theta\bar{\boldsymbol{B}}\right\| \cdot \left\|\hat{\boldsymbol{e}}_{\boldsymbol{LESO}}\right\| \cdot \left|\dot{\Phi}\right| \\
&\le -\lambda_{\min}(\Omega)\left\|\hat{\boldsymbol{e}}_{\boldsymbol{LESO}}\right\|^2 + 2W\left\|\Theta\bar{\boldsymbol{B}}\right\| \cdot \left\|\hat{\boldsymbol{e}}_{\boldsymbol{LESO}}\right\|
\end{aligned} \tag{26}$$

where $\lambda_{\min}(\Omega)$ denotes the smallest eigenvalue of Ω. The condition on $\hat{\boldsymbol{e}}_{\boldsymbol{LESO}}$, when satisfied, ensures that $\dot{V}_0 \le 0$. As a result, LESO remains stable, and the state error sequence of the FSM system converges to zero asymptotically:

$$\left\|\hat{\boldsymbol{e}}_{\boldsymbol{LESO}}\right\| \le \frac{2W\left\|\Theta\bar{\boldsymbol{B}}\right\|}{\lambda_{\min}(\Omega)} \tag{27}$$

therefore, the observer state estimate satisfies:

$$\hat{Z}_1(t) \to y(t), \quad \hat{Z}_2(t) \to \dot{\theta}_v(t), \quad \hat{Z}_3(t) \to \Phi(t) \tag{28}$$

where this equation shows that the LESO estimates converge to the true system states and disturbances when the observation error system is stable. Practically, it verifies LESO's effectiveness: as time progresses, the estimated values Z_1, Z_2, and Z_3 approach the true values x_1, x_2, and x_3, enabling feedforward disturbance compensation and state feedback control.

The Lyapunov function is set as $V = V_1 + V_0$, where $V_1 = \frac{1}{2}s^2$. By solving Equations (18), (19), (23), (26), and (27) simultaneously and differentiating V, the following result is obtained:

$$\begin{aligned}
\dot{V} &= \dot{V}_1 + \dot{V}_0 \\
&= s\begin{bmatrix} \ddot{\theta}_d + P_0x_1 + Q_0x_2 - x_3 - G_0u + \lambda_1 e_2^* \\ +\lambda_2\dfrac{p_1}{q_1}|e_1|^{\frac{p_1}{q_1}-1}\operatorname{sgn}(e_1)e_2^* + \kappa_1 e_1 + \kappa_2\int e_1 dt \end{bmatrix} + \dot{\hat{\boldsymbol{e}}}_{\boldsymbol{LESO}}^{\mathrm{T}}\Theta_{\hat{\boldsymbol{e}}_{\boldsymbol{LESO}}} + \hat{\boldsymbol{e}}_{\boldsymbol{LESO}}^{\mathrm{T}}\Theta_{\dot{\hat{\boldsymbol{e}}}_{\boldsymbol{LESO}}} \\
&\le s\left\{\begin{array}{l} -\dfrac{\varepsilon|e_1|}{k_1 + (1-k_1)e^{-\vartheta|s|}}\tanh(s) - k_2\left[\beta\tanh(|s|) + \dfrac{\phi}{1+\ln(1+\varphi|s|)}\right]s \\ +P_0(x_1 - \hat{Z}_1) + Q_0(x_2 - \hat{Z}_2) + (x_3 - \hat{Z}_3) \end{array}\right\}
\end{aligned} \tag{29}$$

Assume that the state estimation error of the LESO satisfies $\left|x_i - \hat{Z}_i\right| \leq \Psi_i$, where $\Psi_i > 0\ (i = 1,2,3)$. Let $\Psi = \Psi_1 + \Psi_2 + \Psi_3$. Under these conditions, Equation (29) can be further expressed as follows:

$$\begin{aligned} \dot{V} &\leq s\left\{-\frac{\varepsilon|e_1|}{k_1+(1-k_1)e^{-\vartheta|s|}}\tanh(s) - k_2\left[\beta\tanh(|s|) + \frac{\phi}{1+\ln(1+\varphi|s|)}\right]s + \Psi\right\} \\ &\leq \left\{-\frac{\varepsilon|e_1|s}{k_1+(1-k_1)e^{-\vartheta|s|}}\tanh(s) - k_2\left[\beta\tanh(|s|) + \frac{\phi}{1+\ln(1+\varphi|s|)}\right]s^2\right\} \end{aligned} \tag{30}$$

where $\tanh(s)$ has the same sign as s, and $f(e_1, s) > 0$ and $g(s) > 0$, it follows that $\dot{V}_0 \leq 0$. Therefore, the closed-loop control system exhibits asymptotic stability.

According to the basic criterion of finite-time stability [31], for a continuously positive-definite function $F(t) > 0$, if the following differential inequality is satisfied

$$F(t) + vF(t) + \tau F^{\theta}(t) \leq 0, \qquad \forall t > t_0 \tag{31}$$

where $v > 0$, $\tau > 0$ and $0 < \theta < 1$, the function $F(t)$ converges to zero within a finite time t_l, with the upper bound on the convergence time given by:

$$t_l \leq t_0 + \frac{1}{v(1-\theta)}\ln\frac{vF^{1-\theta}(t_0) + \tau}{\tau} \tag{32}$$

Since $f(e_1, s) \geq \varepsilon|e_1|$, $g(s) \geq \frac{\phi}{1+\ln(1+\varphi|s|)}$ and $s \cdot \tanh(s) \geq \frac{s^2}{1+|s|}$, along with the substitutions $V = \frac{1}{2}s^2$ and $|s| = \sqrt{2V}$, the following result can be further derived from Equation (30):

$$\dot{V} \leq -\varepsilon|e_1| \cdot \frac{2V}{1+\sqrt{2V}} - k_2\phi \cdot \frac{2V}{1+\ln\left(1+\varphi\sqrt{2V}\right)} \tag{33}$$

When V is small enough such that $\sqrt{2V} \ll 1$, it follows that $\ln(1+\varphi\sqrt{2V}) \approx \varphi\sqrt{2V}$. In this case, even slight changes in the nonlinear term $\sqrt{2V}$ significantly affect the fractional term. Therefore, $1+\varphi\sqrt{2V}$ can be approximated as $\varphi\sqrt{2V}$, leading to the following expression:

$$\dot{V} + 2\varepsilon|e_1|V + \frac{\sqrt{2}k_2\phi}{\varphi}V^{1/2} \leq 0 \tag{34}$$

By substituting the relevant parameters from Equation (34) into Equation (32), the upper bound for the convergence time of V is obtained as follows:

$$t_l \leq \frac{1}{\varepsilon|e_1|}\ln\frac{2\sqrt{2}\varepsilon\varphi|e_1|V^{1/2}(s_0) + 2k_2\phi}{2k_2\phi} \tag{35}$$

The comprehensive analysis results demonstrate that the control system satisfies both finite-time stability and Lyapunov stability requirements. The sliding mode dynamics will converge to the sliding surface in finite time t_l, i.e., $s = 0$, where s_0 represents the initial state of the proposed controller. Simultaneously, the tracking error state function will also stabilize and converge to zero in finite time, i.e., $e_1 = e_2^* = 0$.

4. Numerical Simulation Validation

In order to prove the usefulness of the control plan suggested, a computer simulation (MATLAB/Simulink) was performed (R2023b). All simulations were executed on a desktop workstation that had the 13th Gen Intel (R) Core (TM) i9-13900HX, 8 GB of DDR5 RAM, and the Windows 11 64-bit operating system, to provide uniform computational performance.

The solver was ode4 (Runge–Kutta method), which was chosen for use due to its trade-off between accuracy and efficiency in solving nonlinear systems. The sampling time was set as 100 μs, which was equivalent to the sampling rate of 10 kHz in the physical experiment, so that the simulation could be synchronized with the real-world system. The integration tolerances were set to 1×10^{-6} to reduce the impact of numerical errors. Other important numerical parameters, such as the fixed-step execution and zero beginning conditions of all system states, remained at default values.

The simulation model of FSM proposes parameters for the system model following those in Equation (40). Empirical adjustment was used to determine all the controller parameters to trade between respondence and accuracy in the control process, but the basic methodology of the tuning involved a series of trials. All simulation controller parameters are represented by specific values that are described in Table 3, and further experiments in simulation will compare the proposed controller with the other four control strategies recommended therein.

Table 3. Parameters of all controllers for numerical simulations.

Controller Modules	Parameters and Values
PID	$K_p = 30$, $K_i = 100$, $K_d = 0.003$
GFTSMC (with CRL)	$\lambda_1 = 900$, $\lambda_2 = 150$, $p_1 = 5$, $q_1 = 7$ $p_0 = 1$, $q_0 = 3$, $k_c = 1500$, $\varepsilon_c = 80$
DIGFTSMC (with CRL)	$\lambda_1 = 900$, $\lambda_2 = 150$, $p_1 = 5$, $q_1 = 7$, $\kappa_1 = 6$, $\kappa_2 = 5$ $p_0 = 1$, $q_0 = 3$, $k_c = 1500$, $\varepsilon_c = 80$
DIGFTSMC (with IARL)	$\lambda_1 = 900$, $\lambda_2 = 150$, $p_1 = 5$, $q_1 = 7$, $\kappa_1 = 6$, $\kappa_2 = 5$ $\varepsilon = 1.9$, $k_1 = 0.9$, $\vartheta = 15$, $k_2 = 7000$ $\beta = 0.8$, $\phi = 2$, $\varphi = 8$
Proposed controller (with IARL)	$\lambda_1 = 900$, $\lambda_2 = 150$, $p_1 = 5$, $q_1 = 7$, $\kappa_1 = 6$, $\kappa_2 = 5$ $\varepsilon = 1.9$, $k_1 = 0.9$, $\vartheta = 15$, $k_2 = 7000$ $\beta = 0.8$, $\phi = 2$, $\varphi = 8$, $r_0 = 5000$, $h_0 = 0.00001$ $\beta_1 = 5000$, $\beta_2 = 7.5 \times 10^7$, $\beta_3 = 1.25 \times 10^{11}$

4.1. Step Response Simulation Experiment

A step response simulation experiment was conducted to measure the accuracy with which the proposed controller would converge dynamically to a steady-state position, and to measure the steadiness of those positioning results. The FSM simulation model was fed with a step input signal of 0 to 1000″ and the key performance measures used were the settling time, the overshoot and steady-state error. The test is a direct indicator of the ability of the controller to respond to sudden reference variations quickly and accurately which is of great importance to high-performance applications involving FSM.

The performance of five control strategies in regard to error and tracking trajectory is indicated by the step response simulation results, as indicated in Figure 7. As noted in Figure 7a, the proposed controller has the quickest rate of tracking response, and it has little overshoot and settling time. Conversely, the PID controller exhibits severe overshoot and moderate convergence. The comparison in Figure 7b shows that the proposed controller has the lowest tracking error, which performs better than the rest of the strategies in magnitude of error. These findings are further supported by the locally magnified images in Figure 7c,d which reveals that the proposed controller holds a smooth and quick approach to the reference signal with decreased steady-state error. These assessment outcomes verify that the proposed controller can be very effective in attaining exact tracking and swift convergence in changing settings.

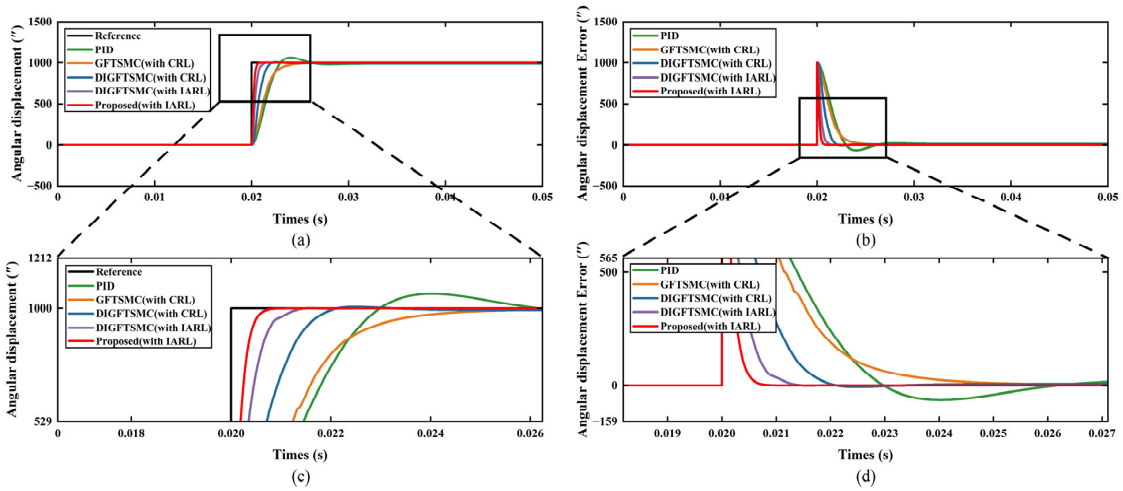


Figure 7. Simulation results of step response experiment. (**a**) Tracking trajectory. (**b**) Tracking error. (**c**) Locally magnified view of tracking trajectory. (**d**) Locally magnified view of tracking error.

4.2. Sinusoidal Signal Tracking Simulation Experiment

To assess the frequency–domain tracking capability and dynamic responsiveness of the proposed controller, a sinusoidal signal tracking simulation was conducted. A sinusoidal input with an amplitude of 300″ and a frequency of 50 Hz served as the reference command, focusing on evaluating the controller's ability to follow periodic trajectories with high precision.

The simulation results of the sinuoidal signal tracking experiment are as given in Figure 8, which compares the performance of five control strategies. Figure 8a indicates the tracking trajectory, and that the proposed controller matches the reference signal closely with low lag, thus abiding by the reference signal and indicating better tracking performance. Conversely, the PID controller has a pronounced phase lag, and slow response. Figure 8b shows the tracking error and that this error is minimized by the proposed controller; it is better than any other approaches based on amplitude and steady-state error. Figure 8c,d, through their locally magnified views, further prove these facts, as it was revealed that the proposed controller can minimize tracking lag and ensure low error during the tracking process. This shows that this proposed controller is able to achieve a good and correct tracking performance in dynamic signal processing.

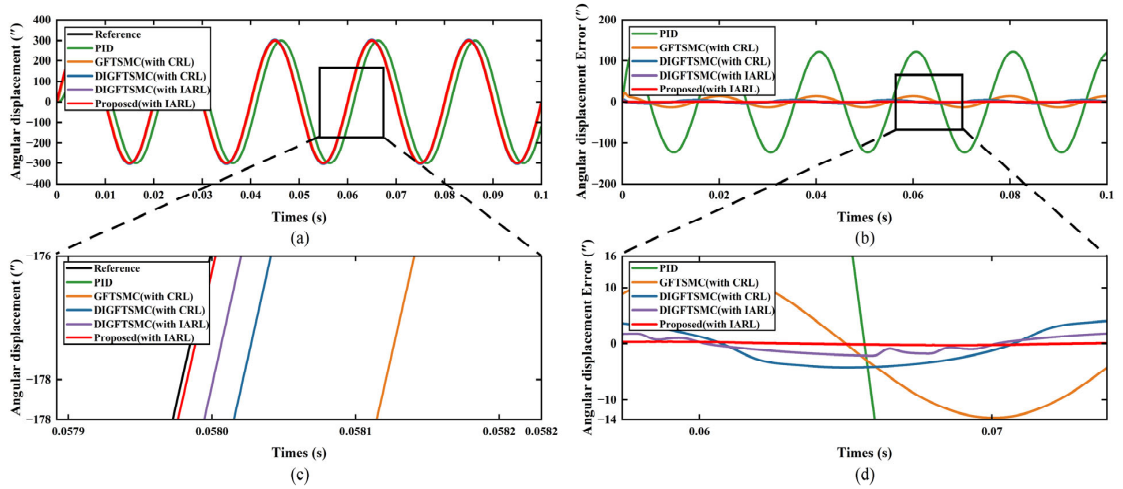


Figure 8. Simulation results of sinusoidal signal tracking experiment. (**a**) Tracking trajectory. (**b**) Tracking error. (**c**) Locally magnified view of tracking trajectory. (**d**) Locally magnified view of tracking error.

4.3. Multi-Sinusoidal Signal Tracking Simulation Experiment

To further assess the tracking performance of the proposed controller, a multi-sinusoidal signal tracking experiment was conducted. The reference signal was defined as $\theta_d = 100\sin(2\pi \cdot 50t) + 300\sin(2\pi \cdot 100t) + 250\cos(2\pi \cdot 150t) + 200\cos(2\pi \cdot 200t)$, consisting of multiple frequency components. This simulation tested the controller's ability to accurately track a composite signal with varying frequencies and amplitudes, assessing its robustness and precision in handling real-world dynamic inputs.

The simulation result of the multi-sinuoidal signal tracking experiment in Figure 9 is used to test the sample of the five control strategies under a more complex input signal formed by a number of frequencies. The tracking trajectory, as shown in Figure 9a, shows that the proposed controller is effective in its management of the dynamic changes amongst the various frequency components of the reference signal and keeps its tracking accurate and continuous. However, the PID controller undergoes the poorest characteristics, and tracking errors and phase discrepancy are bigger, particularly with varying frequency components. Figure 9b indicates the error in the tracking as the proposed controller demonstrates the best ability to minimize the steady-state error as compared to the other sliding mode controllers. The same views (Figure 9c,d), locally magnified, further support the fact that the proposed controller is capable of reducing the effect of transient errors and dealing with high-frequency variations with much better accuracy. These findings substantiate that the proposed controller is very good at tracking multi-sinusoidal signals, and very high performance is still obtained even with dynamic conditions of different frequencies and amplitudes, and the interplay between these proves the robustness and adaptability of the controller to complex dynamic inputs with a different frequency and amplitude.

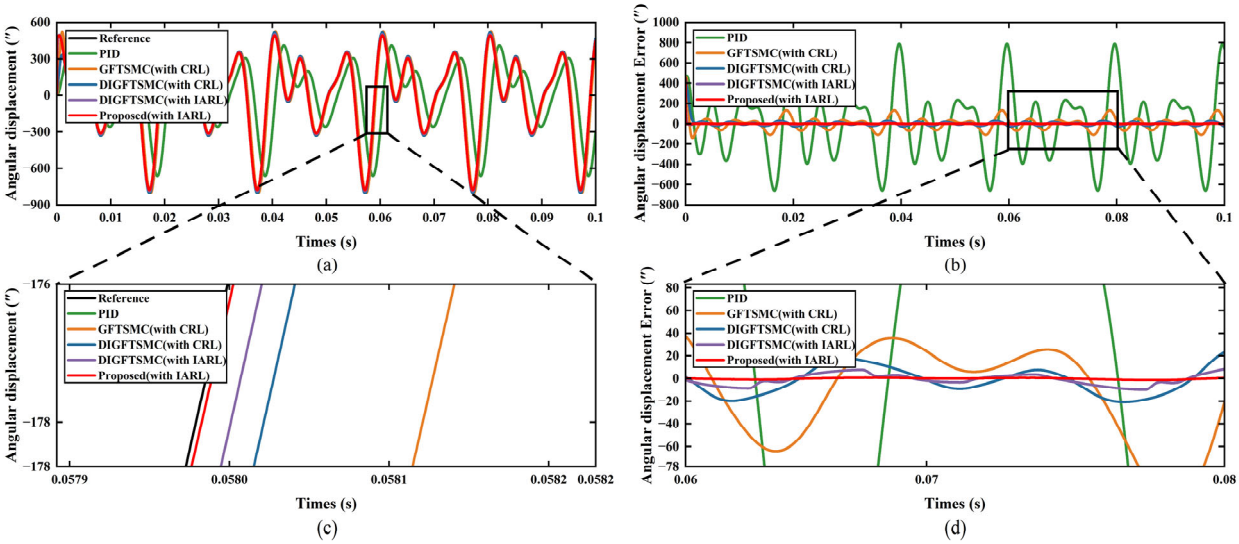


Figure 9. Simulation results of multi-sinusoidal signal tracking experiment. (**a**) Tracking trajectory. (**b**) Tracking error. (**c**) Locally magnified view of tracking trajectory. (**d**) Locally magnified view of tracking error.

4.4. Random Vibration Disturbance Rejection Simulation Experiment

In order to determine the disturbance rejection capacity of the proposed controller in the presence of stochastic perturbation, we performed a simulation test of resistance to random vibration disturbance. The FSM model had been subjected to a step input of 0 to 1000″ with random disturbances of high frequency that were simulated using white noise (power = 0.0001, sampling time = 0.00001) at random positions over the response process. The test focuses on tracking performance of each controller after reaching the 1000″

steady state, validating the proposed controller's ability to maintain tracking precision and dynamic stability amid random disturbances.

Figure 10 shows the simulation outputs of the experiment of random vibration disturbance rejection where the performance of five control strategies is evaluated during the a disturbance of high frequency. Figure 10a plots the tracking trajectory, in which the proposed controller maintains the closest alignment with the reference signal, thus verifying its superior disturbance rejection capability. In contrast, the other control strategies exhibit varying degrees of deviation and distinct recovery dynamics, with their performance deteriorating markedly as the disturbance intensifies. The tracking errors are illustrated in Figure 10b, which demonstrates that the proposed controller consistently yields the minimum error magnitude and outperforms the comparative strategies in terms of steady-state accuracy. The DIGFTSMC approach with only IARL also shows some improvement over the PID controller, but still experiences noticeable tracking errors during disturbances. The locally magnified views in Figure 10c,d further demonstrate the superior performance of the proposed controller, with minimal fluctuations and fast recovery from disturbances, thanks to the precise disturbance estimation and compensation enabled by the LESO. Additionally, the double-integral sliding mode structure and IARL help to reduce error by accelerating the system's convergence to the reference signal, effectively eliminating steady-state error and improving disturbance rejection.

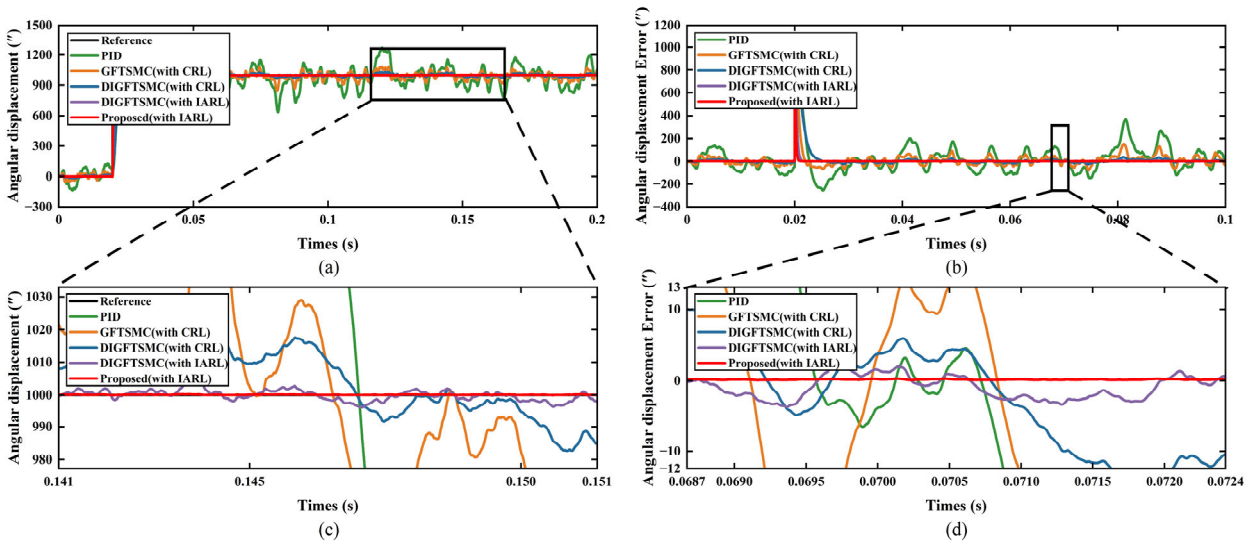
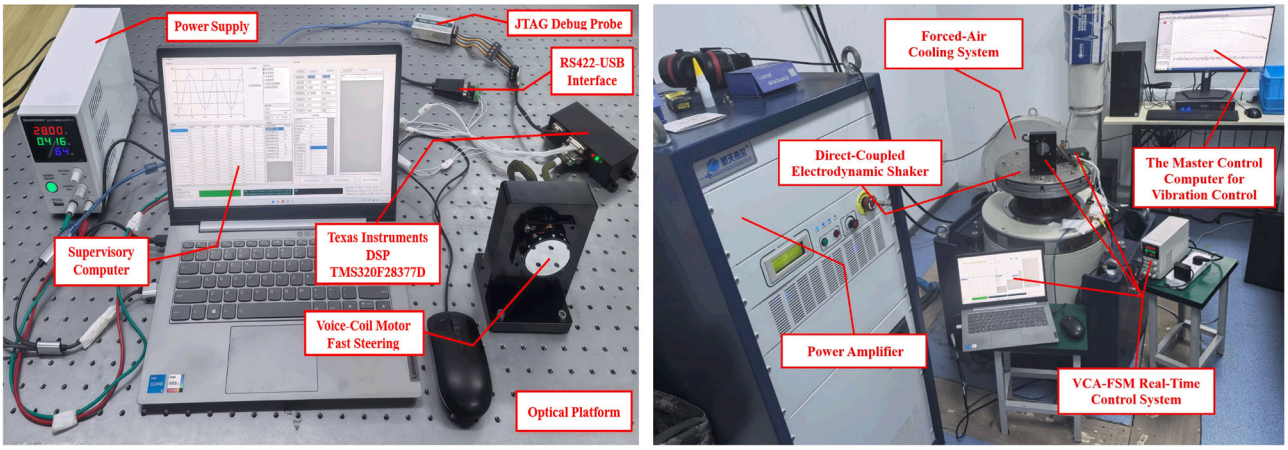


Figure 10. Simulation results of random-vibration disturbance rejection experiment. (**a**) Tracking trajectory. (**b**) Tracking error. (**c**) Locally magnified view of tracking trajectory. (**d**) Locally magnified view of tracking error.

5. Experimental Verification

To evaluate the practical control performance and disturbance rejection capability of the proposed controller, a real-time control and vibration testing platform based on an embedded system was developed. The experimental setup is shown in Figure 11a,b. The platform uses a voice coil motor FSM with a 1-inch diameter and a ±26.2 mrad scan range as the core actuator. The main controller is a TMS320F28377D Digital Signal Processor (DSP), responsible for executing the control algorithm. In the feedback loop, signals from the eddy current sensor are sampled at 10 kHz by an ADC module and fed to the DSP. The control commands are issued by a host computer through an RS422 serial communication interface, then processed by a 16-bit DAC and a power amplification circuit to drive the FSM for the desired deflection. The actual mirror angle is continuously measured by the eddy current sensor, providing closed-loop feedback.



(a) (b)

Figure 11. Voice coil motor fast steering mirror experimental test environment. (**a**) Real-time control test. (**b**) Random vibration disturbance rejection test.

The vibration experiments were performed using a direct-coupled electrodynamic shaker manufactured by Beijing ETS Solutions LTD. The shaker system consisted of an L620M shaker body and an MPA102 power amplifier. It operates over a nominal frequency range of 2–3500 Hz, while the practical test frequency range was limited to 20–2000 Hz, and provides a rated random excitation force of 6 kN, which is sufficient to ensure stable and repeatable excitation for high-frequency dynamic performance evaluation.

In this section, we evaluate the performance of the proposed controller for different reference input signals quantitatively. For step input signals, the following evaluation indices are considered: settling time (the time required for the system output to settle within the band $\pm 5\%$ around the steady-state value), mean absolute error (MAE) and root mean square error (RMSE). For sine input signals, multi-sinusoidal signals, and the random vibration disturbance rejection test, the maximum error (MAXE), MAE and RMSE are considered for quantitative characterization, respectively. The mathematical formulas of the above quantitative evaluation indices are given as follows.

$$T_s = \inf\{t \geq 0 : \ |c(v) - c_{ss}| \leq 0.05 \cdot |c_{ss}|, \quad \forall v \geq t\} \tag{36}$$

$$\text{MAXE} = \max|e_1(k)|, \quad k \in [0, N] \tag{37}$$

$$\text{MAE} = \frac{1}{N}\sum_{k=1}^{N}|e_1(k)| \tag{38}$$

$$\text{RMSE} = \sqrt{\frac{1}{N}\sum_{k=1}^{N} e_1(k)^2} \tag{39}$$

In order to make a fair comparison, we have picked four strategies of sliding mode control: GFTSMC and DIGFTSMC using CRL, DIGFTSMC using IARL and the proposed controller. The choice is meant to evaluate how the double-integral structure, IARL, and LESO are effected on the performance of the system. Taking into account the real life limitations of the system, we adjusted all the parameters of controllers with the help of massive experimentation. Table 4 illustrates the specifications of these controller parameters.

Table 4. Parameters of all controllers for experimental tests.

Controller Modules	Parameters and Values
PID	$K_p = 10$, $K_i = 0.015$, $K_d = 0.0025$
GFTSMC (with CRL)	$\lambda_1 = 650$, $\lambda_2 = 120$, $p_1 = 5$, $q_1 = 7$ $p_0 = 1$, $q_0 = 3$, $k_c = 1300$, $\varepsilon_c = 100$
DIGFTSMC (with CRL)	$\lambda_1 = 650$, $\lambda_2 = 120$, $p_1 = 5$, $q_1 = 7$, $\kappa_1 = 3$, $\kappa_2 = 2$ $p_0 = 1$, $q_0 = 3$, $k_c = 1300$, $\varepsilon_c = 100$
DIGFTSMC (with IARL)	$\lambda_1 = 650$, $\lambda_2 = 120$, $p_1 = 5$, $q_1 = 7$, $\kappa_1 = 3$, $\kappa_2 = 2$ $\varepsilon = 1$, $k_1 = 0.3$, $\vartheta = 20$, $k_2 = 8000$ $\beta = 1.2$, $\phi = 5$, $\varphi = 10$
Proposed controller (with IARL)	$\lambda_1 = 650$, $\lambda_2 = 120$, $p_1 = 5$, $q_1 = 7$, $\kappa_1 = 3$, $\kappa_2 = 2$ $\varepsilon = 1$, $k_1 = 0.3$, $\vartheta = 20$, $k_2 = 8000$ $\beta = 1.2$, $\phi = 5$, $\varphi = 10$, $r_0 = 2000$, $h_0 = 0.0002$ $\beta_1 = 1000$, $\beta_2 = 3 \times 10^6$, $\beta_3 = 1 \times 10^9$

For the parameter tuning of the proposed controller, specific guidelines were followed: the sliding mode linear gains λ_1 and λ_2 need to be sufficiently large to dominate the system dynamics far from equilibrium and accelerate convergence under large errors; the integral coefficients κ_1 and κ_2 must balance steady-state error elimination, as excessive values induce integral saturation or overshoot while insufficient values slow error attenuation; the IARL parameters ε, ϑ, k_1, k_2, β, ϕ, and sliding mode nonlinear exponent p_1/q_1 require a trade-off between convergence speed and chattering suppression, where ε and ϑ regulate the adaptive gain amplitude, k_1 and k_2 adjust the gain variation rate and reaching speed, β provides linear damping, ϕ and φ optimize smooth convergence near the sliding surface, with p_1/q_1 satisfying $0 < p_1/q_1 < 1$ to guarantee finite-time convergence near the equilibrium point and sliding surface smoothness; the LESO parameters β_1, β_2, and β_3 are derived based on the observer bandwidth ω_0 via Equation (13) to meet stability criteria; the TD parameters r_0 and h_0 are selected according to transient smoothness requirements. The final parameters for the proposed controller were determined through a trial-and-error approach under these constraints, consistent with the parameter optimization process applied to the comparative control strategies.

A sensitivity analysis was performed by varying key parameters of the proposed controller around their optimal values to evaluate performance robustness. For sliding mode linear gains λ_1 and λ_2 excessive values enhanced convergence speed with large errors but may induce overshoot, while insufficient values degrade dynamic response and tracking accuracy. Integral coefficients κ_1 and κ_2 exhibit sensitivity related to steady-state error and overshoot balance—deviations from optimal values either trigger integral saturation or leave residual steady-state errors. Regarding IARL parameters, variations in ε and ϑ affect adaptive gain amplitude and thus chattering levels; adjustments to k_1 and k_2 alter gain variation rate and reaching speed with trade-offs in dynamic smoothness; changes in β influence linear damping effects, while ϕ and φ show low sensitivity as their deviations barely impact smooth convergence near the sliding surface. For sliding mode nonlinear exponent p_1/q_1, deviations from the optimal range compromise finite-time convergence near equilibrium and sliding surface smoothness. LESO parameters β_1, β_2, and β_3, which are derived from observer bandwidth ω_0, exhibit sensitivity to disturbance estimation performance, where excessive ω_0 amplifies sensor noise and chattering, while insufficient values impair disturbance rejection capability. TD parameters r_0 and h_0 affect transient smoothness and tracking speed, with deviations leading to either overshoot or delayed response. Collectively, these results confirm the controller's robustness to moderate parameter perturbations, validating the rationality of the proposed parameter tuning guidelines.

5.1. System Model Parameter Identification

The frequency sweep technique is employed in the determination of the linear dynamic model of the FSM system. An excitation signal of fixed amplitude that has a linearly varying frequency is used. The model is fitted to the response data using the MATLAB system identification toolbox which gives a goodness-of-fit of 88.96% with the experimental data (Figure 12). This finding proves that the model is quite appropriate in reflecting the main linear dynamic nature of this system thus a model that can be relied upon in the development of the high-performance control algorithms.

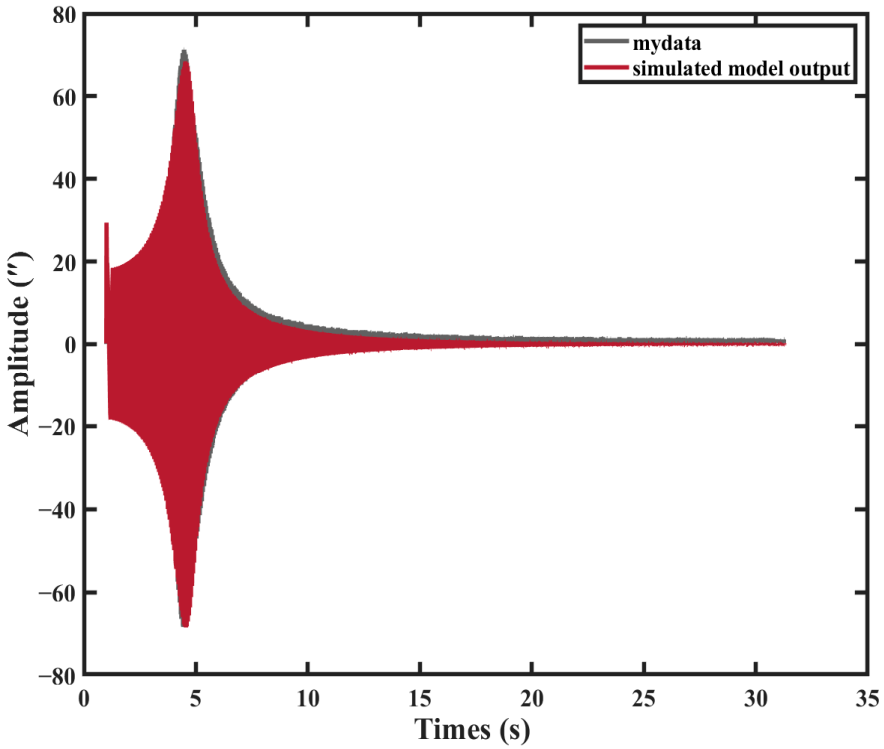


Figure 12. Parameter identification validation plot for VCM-FSM system model.

The MATLAB system identification toolbox employs the least squares method to determine the parameters of the FSM system model. Consequently, the open-loop transfer function of the voice coil motor FSM system is derived as follows:

$$G(s)=\frac{\theta(s)}{U(s)}=\frac{73780}{s^2+102s+144600} \tag{40}$$

where $P_0=\frac{K_s}{J_m}=144600, Q_0=\frac{RB_m+K_tK_e}{RJ_m}=102,$ and $G_0=\frac{K_t}{RJ_m}=73780.$

The full-state constraints for the voice-coil motor-driven FSM are determined based on the system's physical limits and dynamic performance requirements: angular deflection (±26.2 mrad) is bounded by the flexible hinge's mechanical stroke and optical path interference avoidance; angular velocity and acceleration are constrained by the voice coil motor's thrust capacity and its structural strength to prevent fatigue failure; motor drive current and voltage adhere to the actuator's rated parameters and thermal dissipation limits; structural stability constraints are defined to mitigate dynamic instability. These constraints align with the proposed controller's feasible region, ensuring the system's safe and high-precision operation.

5.2. Step Response Test

In order to test the dynamic response and positioning capability of the proposed controller, a step command 0 to 1000″ was inputted on the FSM system using the upper computer. The experimental results (Figure 13a–c) prove that all of the control strategies are able to adhere to the step command. It is important to note that this proposed controller has the fastest steady-state convergence, which significantly improves the accuracy of control and stability in the steady-state performance and effectively eliminates the error fluctuations and high-frequency chattering. Contrarily, the GFTSMC approach with only CRL has a slow response and steady-state error between 2 and 3% since it does not have an efficient reaching law, double-integral, and disturbance observation combinations. A quantitative assessment (Figure 14) indicates that the settling time of the proposed controller value is only 1.6 ms which is 81.0% and 48.4% lower than the PID controller and the DIGFTSMC approach with only IARL, respectively. In addition, the MAE and the RMSE values are also significantly smaller. Moreover, Figure 13d illustrates the role that the LESO plays in disturbance estimation, i.e., it may be considered that the observer keeps the original zero-position balance of the FSM system intact prior to the initiation of the command. Although there was a short-lived deviation after giving the step command, it quickly regains focus towards and follows the actual disturbance exactly, which exhibits superior dynamic estimation and convergence qualities. Overall, the proposed controller has significant advantages when it comes to dynamic response and steady-state accuracy. Notably, the experimental results of the step response are consistent with the trends of the numerical simulation experiment, both verifying the proposed controller's superiority in fast convergence and high-precision positioning.

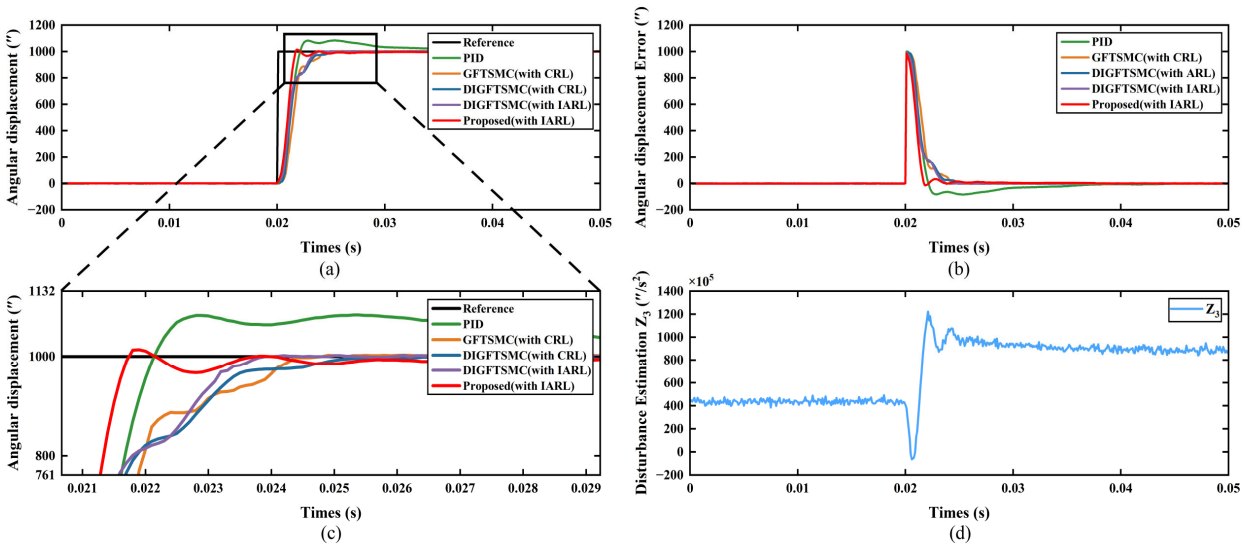


Figure 13. Experimental results of step response test. (**a**) Tracking trajectory. (**b**) Tracking error. (**c**) Locally magnified view of tracking trajectory. (**d**) Disturbance estimation Z_3 by the LESO.

Figure 15 provides further insight into the internal control behavior during the step response by illustrating the time histories of the control input torque and the adaptive gains incorporated in the IARL.

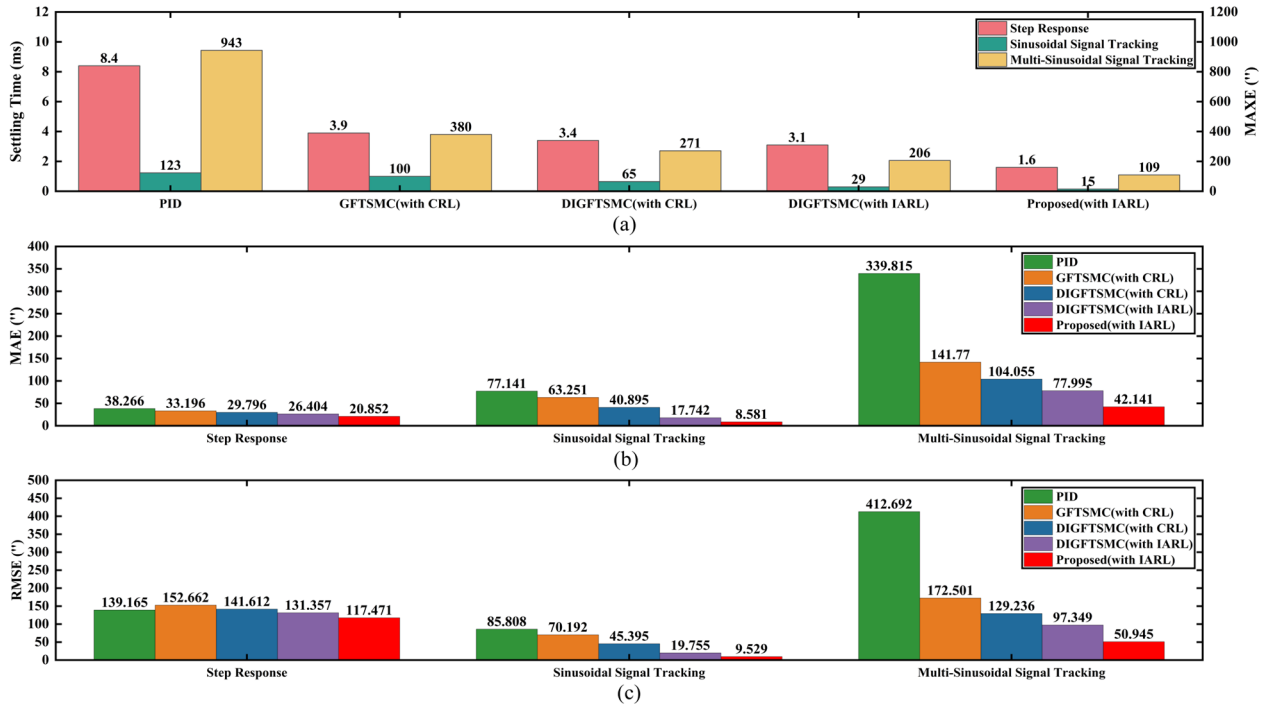


Figure 14. Quantitative analysis of the step response, sinusoidal signal tracking and multi-sinusoidal signal tracking tests. (**a**) Settling time and MAXE. (**b**) MAE. (**c**) RMSE.

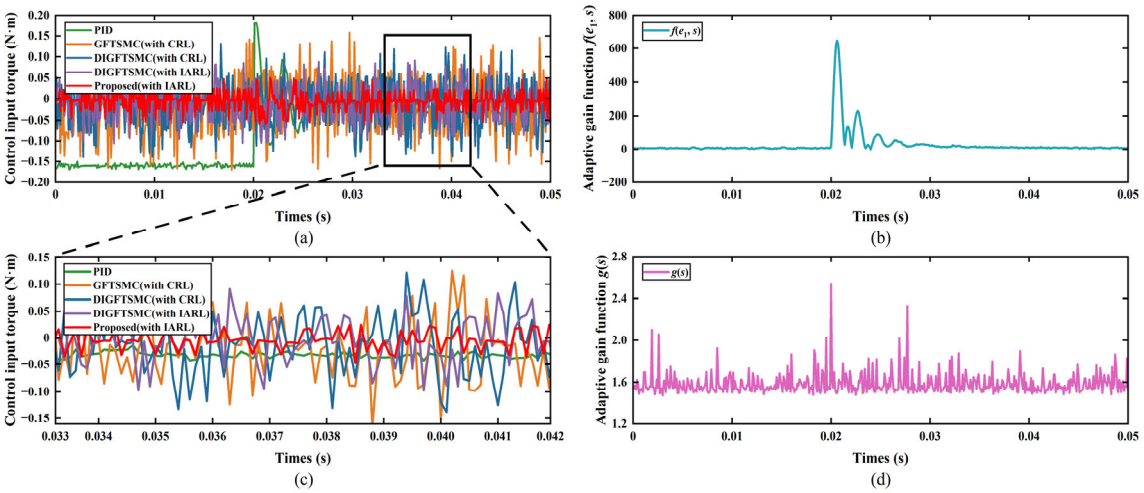


Figure 15. Experimental results of control input and adaptive gain responses under step response. (**a**) Control input torque. (**b**) Adaptive gain function $f(e_1, s)$ in the IARL. (**c**) Locally magnified view of control input torque. (**d**) Adaptive gain function $g(s)$ in the IARL.

As shown in Figure 15a, the proposed controller generates a significantly smoother and lower-amplitude control torque compared with the PID controller and conventional sliding-mode-based schemes. Although transient fluctuations appear immediately after the step command, the torque rapidly settles within a narrow-bounded range, indicating effective suppression of high-frequency chattering. The locally magnified view in Figure 15c further confirms that the proposed controller avoids abrupt switching behavior while maintaining sufficient control authority. Figure 15b,d depict the time evolution of the adaptive gain functions $f(e_1, s)$ and $g(s)$, respectively. It can be observed that $f(e_1, s)$ exhibits a sharp but short-lived increase during the initial transient phase, providing strong corrective action when the tracking error is large. As the system approaches steady state, the gain

automatically decreases, preventing excessive control effort. Meanwhile, $g(s)$ remains bounded and slowly varying, ensuring smooth convergence of the sliding variable without introducing instability.

These results demonstrate that the IARL dynamically balances rapid error attenuation and control smoothness, thereby explaining the superior transient performance and reduced chattering observed in the step response.

5.3. Sinusoidal Signal Tracking Test

To determine the performance of the proposed controller in the frequency domain tracking, the FSM system was excited by writing a sinusoidal signal to the host computer with an amplitude of 300″ and a frequency of 50 Hz. Figure 16a shows that all of the control strategies have the ability to track sinusoidal signals generally, but the performance of the PID controller is significantly poorer compared to the rest of the sliding mode control strategies. Figure 16b highlights that the proposed controller exhibits the smallest tracking error, demonstrating superior accuracy. This accuracy is attributed to the double integral terms, IARL, TD smoothing reference signal, and LESO's effective disturbance compensation (Figure 16d). Quantitative analysis in Figure 14 reveals that the proposed controller's MXE, MAE, and RMSE are 15″, 8.581″, and 9.529″, respectively. Compared to the PID controller, the MAE and RMSE are reduced by 88.9%. In comparison to the DIGFTSMC approach with only IARL, reductions are 51.6% and 51.8%, respectively. These experimental results confirm that the proposed controller can accurately track continuous trajectories at a specified frequency, showcasing excellent dynamic response and robustness. The superior tracking performance observed in the experiment is consistent with the trends of the sinusoidal signal tracking simulation, both validating the proposed controller's strong frequency–domain adaptability and low tracking error.

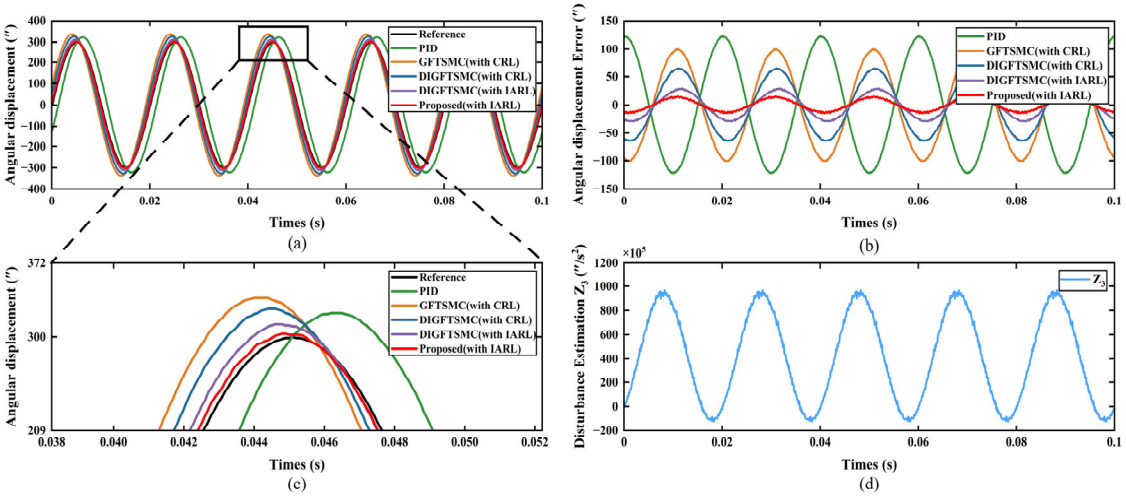


Figure 16. Experimental results of 50 Hz sinusoidal signal tracking test. (**a**) Tracking trajectory. (**b**) Tracking error. (**c**) Locally magnified view of tracking trajectory. (**d**) Disturbance estimation Z_3 by the LESO.

To further analyze the controller behavior under continuous dynamic excitation, Figure 17 presents the control input torque and adaptive gain responses during sinusoidal signal tracking.

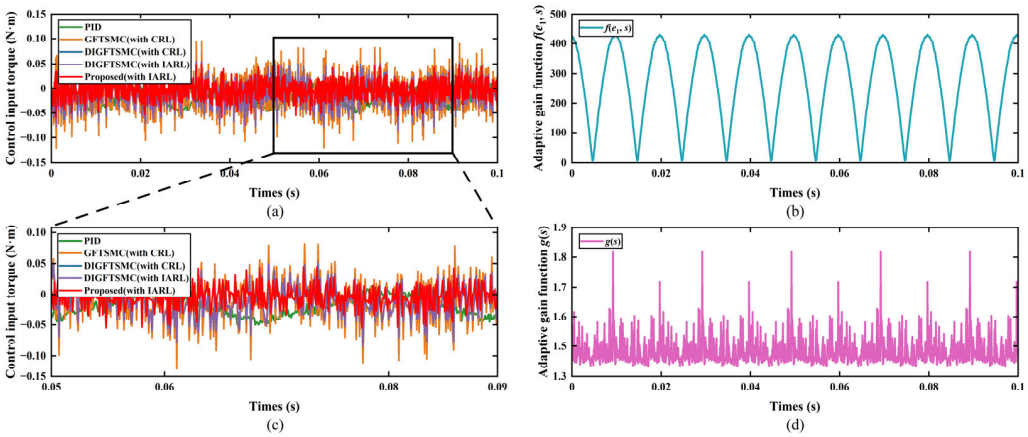


Figure 17. Experimental results of control input and adaptive gain responses under sinusoidal signal tracking. (**a**) Control input torque. (**b**) Adaptive gain function $f(e_1, s)$ in the IARL. (**c**) Locally magnified view of control input torque. (**d**) Adaptive gain function $g(s)$ in the IARL.

The input of the proposed controller is a quasi-periodic control torque following closely the sinusoidal reference with significantly smaller fluctuations in the amplitude than the other control strategies as shown in Figure 17a. The enlarged view in Figure 17c reveals that the torque waveform remains smooth and well-regulated, indicating that the double-integral structure and IARL are effective in reducing chattering even during the continuous oscillatory motion. The corresponding adaptive gain trajectories are shown in Figure 17b,d. The gain function $f(e_1, s)$ is periodically modulated with the dynamics of the tracking error, giving higher control action at the extremes of the error and less control action at the correlating points of zero-crossing. In contrast, $g(s)$ maintains a bounded and slowly varying profile, which contributes to stable sliding-mode evolution and prevents excessive gain amplification.

These observations confirm that the IARL mechanism enables the controller to adaptively regulate control effort in real time, achieving high tracking accuracy with reduced control energy under sinusoidal excitation.

5.4. Multi-Sinusoidal Signals Tracking Test

In the tests to evaluate the tracking capacity and performance of the proposed controller under a dynamic and uncertain environment, we used a composite signal in the form of multi-frequency harmonics as the reference signal. The composite reference trajectory is as defined below:

$$\theta_d = 100\sin(2\pi \cdot 50t) + 300\sin(2\pi \cdot 100t) + 250\cos(2\pi \cdot 150t) + 200\cos(2\pi \cdot 200t) \quad (41)$$

As demonstrated by the experimental findings (Figure 18a), the PID controller has the poorest tracking accuracy. Contrarily, although all of the four sliding mode controllers are capable of tracking the complicated paths in a stable state, the proposed controller stands out by exhibiting the least amount of error fluctuation (Figure 18b). It converges quickly and follows the target path precisely even with harsh signal structures and extreme dynamic transitions. The quantitative analysis (Figure 14) shows that the proposed controller decreases the MAE by 87.6% and 46.0% compared to the PID controller and the DIGFTSMC approach with only IARL, respectively, and decreases the RMSE by 87.7% and 47.7%. The obtained results validate the proposed controller's high precision and strong behavior in following complicated dynamic paths, and thus its efficiency in tackling the complicated dynamic input issues found in real-world engineering. This experimental performance is highly consistent with the trends of the multi-sinusoidal signal tracking simulation, where

the proposed controller also showed minimal error fluctuations and superior adaptability with complex dynamic inputs.

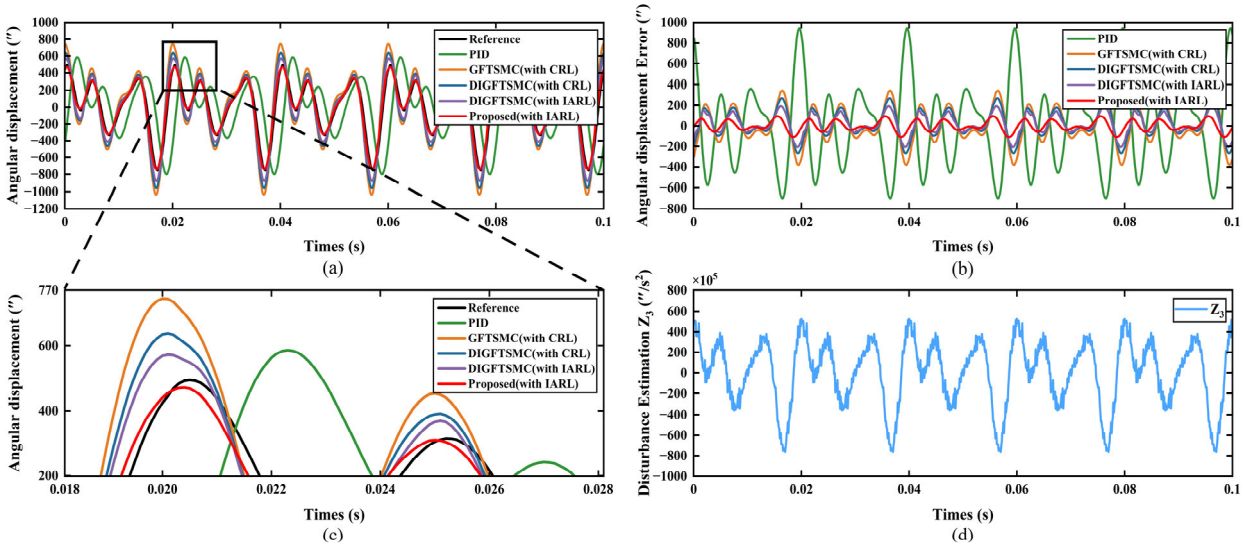


Figure 18. Experimental results of multi-sinusoidal signal tracking test. (**a**) Tracking trajectory. (**b**) Tracking error. (**c**) Locally magnified view of tracking trajectory. (**d**) Disturbance estimation Z_3 by the LESO.

To characterize the controller's response to a stochastically varying, irregular reference trajectory, Figure 19 presents the time histories of the control's input torque together with the IARL adaptive gains during random bits of pronounced low-frequency oscillations with intermittent large excursions, whereas the other sliding-mode schemes still present scattered high-frequency fluctuations. By contrast, the torque generated by the proposed controller remains confined within a more narrowly bounded range, indicating that the control action is delivered in a smoother manner even when the reference changes irregularly. The locally enlarged view in Figure 19c further confirms that the proposed controller avoids abrupt switching and torque bursts, thereby alleviating chattering while preserving sufficient actuation authority to accommodate stochastic variations.

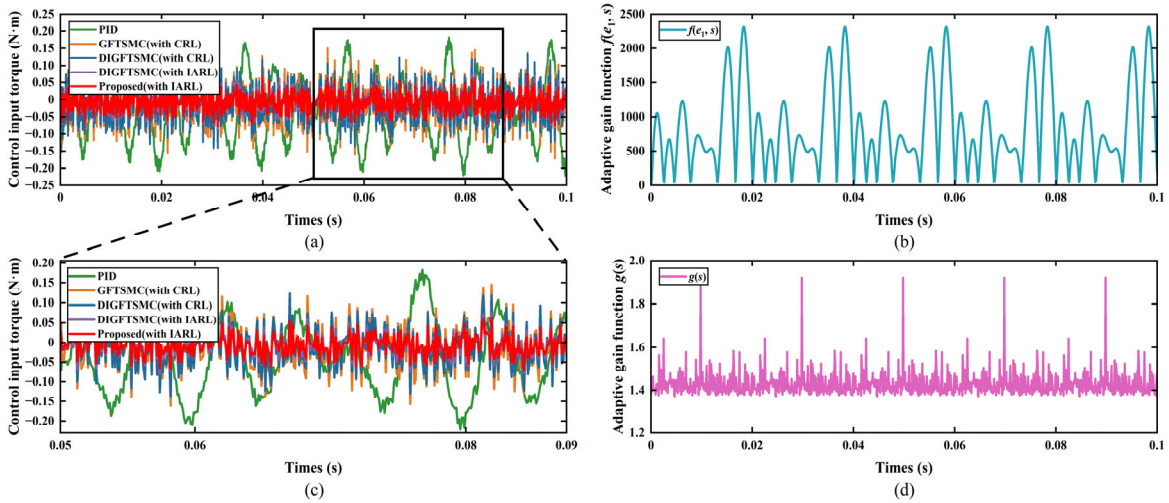


Figure 19. Experimental results of control input and adaptive gain responses under multi-sinusoidal signal tracking. (**a**) Control input torque. (**b**) Adaptive gain function $f(e_1, s)$ in the IARL. (**c**) Locally magnified view of control input torque. (**d**) Adaptive gain function $g(s)$ in the IARL.

The corresponding adaptive gain evolutions are provided in Figure 19b,d. It can be observed that $f(e_1, s)$ exhibits intermittent, short-duration peaks, which can be interpreted as an "on-demand" reinforcement activated by sudden increases in the tracking error or the sliding deviation under random excitation. Following each peak, the gain decreases promptly, thereby avoiding a persistently high gain that could lead to unnecessarily large control effort. Meanwhile, $g(s)$ remains bounded at a relatively low level with occasional sharp spikes, indicating a mild yet effective adjustment of the reaching dynamics that promotes timely correction while maintaining smooth control evolution.

These results indicate that the IARL mechanism adaptively adjusts the control input's intensity according to the instantaneous difficulty of the random tracking. This dynamic balance explains why the proposed controller can maintain robust tracking performance in stochastic conditions while simultaneously reducing torque chattering and avoiding unnecessary actuation energy.

5.5. Random Vibration Disturbance Rejection Test

In order to compare the operation of four sliding mode control strategies under disturbance conditions, the reference trajectory is defined as being $\theta_d = 1000''$. Once the system reaches a steady state, a random vibration with a power spectral density as shown in Figure 20b is introduced to the vibration platform via the master computer panel of control. This is a simulation of external shocks which an FSM can undergo in a real working environment.

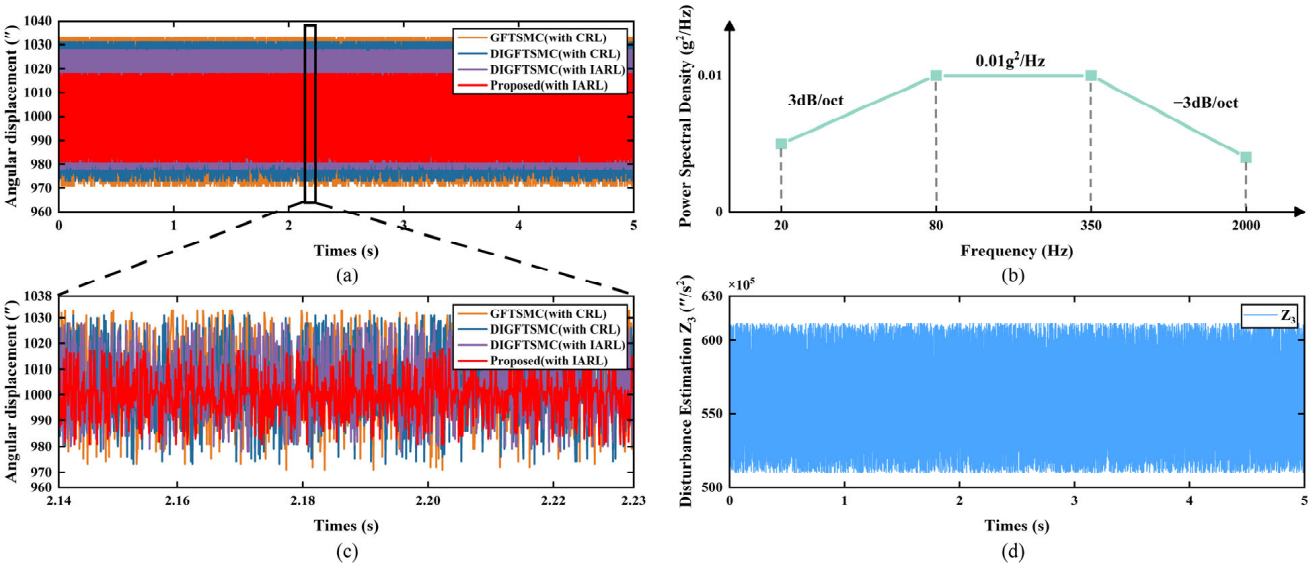


Figure 20. Experimental results of the first random vibration disturbance rejection test. (**a**) Tracking trajectory. (**b**) Random vibration screening spectrum. (**c**) Locally magnified view of tracking trajectory. (**d**) Disturbance estimation Z_3 by the LESO during the 1st test.

Figure 20a presents the results of the first random vibration test. The results show that the effectiveness of the suggested controller in reducing the random vibration disturbances is huge. It is indicated that the controller has better success in tracking the position and stability of the system compared to the compared sliding mode control methods illustrated in Figure 20a,c. Its angular displacement variation is essentially knocked out within 31″ and the average reduction is more than 44% greater than the other techniques, demonstrating its better disturbance rejection ability. This performance gain is largely explained by the fact that lumped disturbances are properly estimated by the LESO (Figure 20d) and that the presence of the double-integral terms in the sliding surface also causes the composite

control method to not only detect, but also mitigate the complex random vibrations within the system, thereby bettering the overall control precision and gains in the system. These findings support the usefulness and practicability of the proposed controller in settings with high vibration acceptance and hard control execution. The excellent disturbance rejection performance in this experiment is consistent with the trends of the random vibration disturbance rejection simulation, both verifying the proposed controller's strong ability to suppress random vibrations and maintain stable tracking.

To enhance the reproducibility and experimental rigor of the random vibration study, and to strengthen the credibility of the proposed control algorithm in terms of disturbance rejection, two additional random vibration tests were conducted under identical experimental conditions and parameter settings.

Figure 21a–d compare the tracking trajectories of the proposed controller against the other sliding mode control schemes during the second and third random vibration tests, while Figure 21e,f present the corresponding LESO disturbance estimates Z_3. As shown in Figure 21a,b, all controllers maintain bounded tracking under stochastic excitation; however, the proposed controller exhibits markedly narrower angular displacement fluctuations and a more compact trajectory envelope. The enlarged views in Figure 21c,d further reveal that, in the high-frequency vibration interval around 2.22–2.32 s, the proposed controller suppresses rapid oscillations more effectively, yielding smoother responses with reduced peak-to-peak variations compared with the GFTSMC and DIGFTSMC approaches with only CRL, as well as the DIGFTSMC approach with only IARL. This improvement indicates enhanced robustness and faster disturbance accommodation under severe random inputs. Moreover, the disturbance estimates in Figure 21e,f demonstrate that the LESO embedded in the proposed controller provides a stable and continuous estimation of the lumped disturbance Z_3 throughout both tests, without noticeable drift or divergence. Together, these results confirm that the synergistic integration of IARL, double-integral terms, and LESO significantly strengthens real-time disturbance rejection, leading to superior tracking stability and consistency in random vibration environments.

Figure 22a–c quantitatively demonstrate that the superior disturbance rejection and tracking accuracy of the proposed controller under three independent random vibration tests, as evaluated by MAX, MAE, and RMSE. In terms of MAX, the proposed controller consistently achieves lowest values of 19″, 17″, and 20″, compared with the GFTSMC approach with only CRL (33″–36″), the DIGFTSMC approach with only CRL (30″–31″), and the DIGFTSMC approach with only IARL (27″–28″), corresponding to a maximum reduction of over 44%. Similar trends are observed for MAE, where the proposed controller limits the average error to 6.645″, 6.359″, and 6.692″, representing reductions of approximately 37–41% relative to the DIGFTSMC approach with only IARL. The RMSE results further confirm this advantage, with values tightly bounded around 8.0″–8.7″, whereas the other approaches remain above 13.8″ in all tests. The general pattern of these gradual positive changes in all metrics and test cases suggests that the proposed control scheme contributes to significantly better robustness to stochastic disturbances of vibration, which leads to a subsequent augmentation of disturbance attenuation capacity and enhanced closed-loop stability under random excitation.

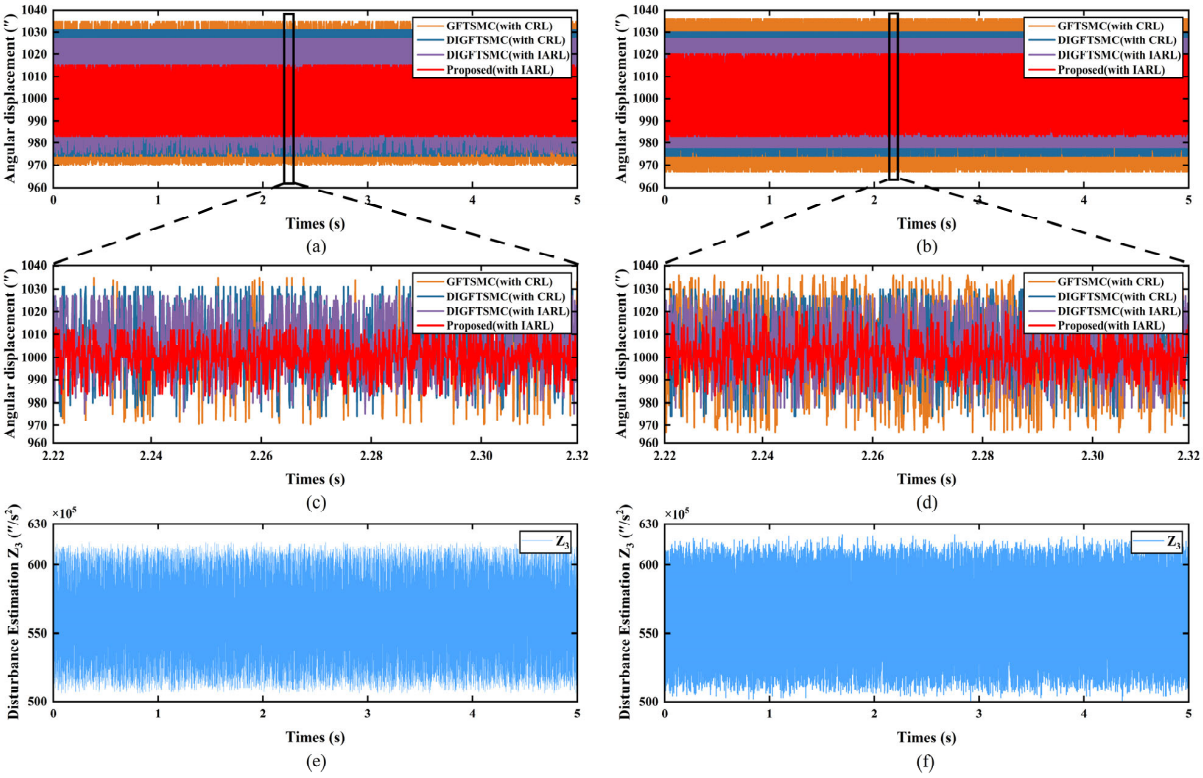


Figure 21. Experimental results of the second and third random vibration disturbance rejection tests. (**a**) Tracking trajectory under the 2nd random vibration test. (**b**) Tracking trajectory under the 3rd random vibration test. (**c**) Locally magnified view of tracking trajectory. (**d**) Locally magnified view of tracking trajectory. (**e**) Disturbance estimation Z_3 by the LESO during the 2nd test. (**f**) Disturbance estimation Z_3 by the LESO during the 3rd test.

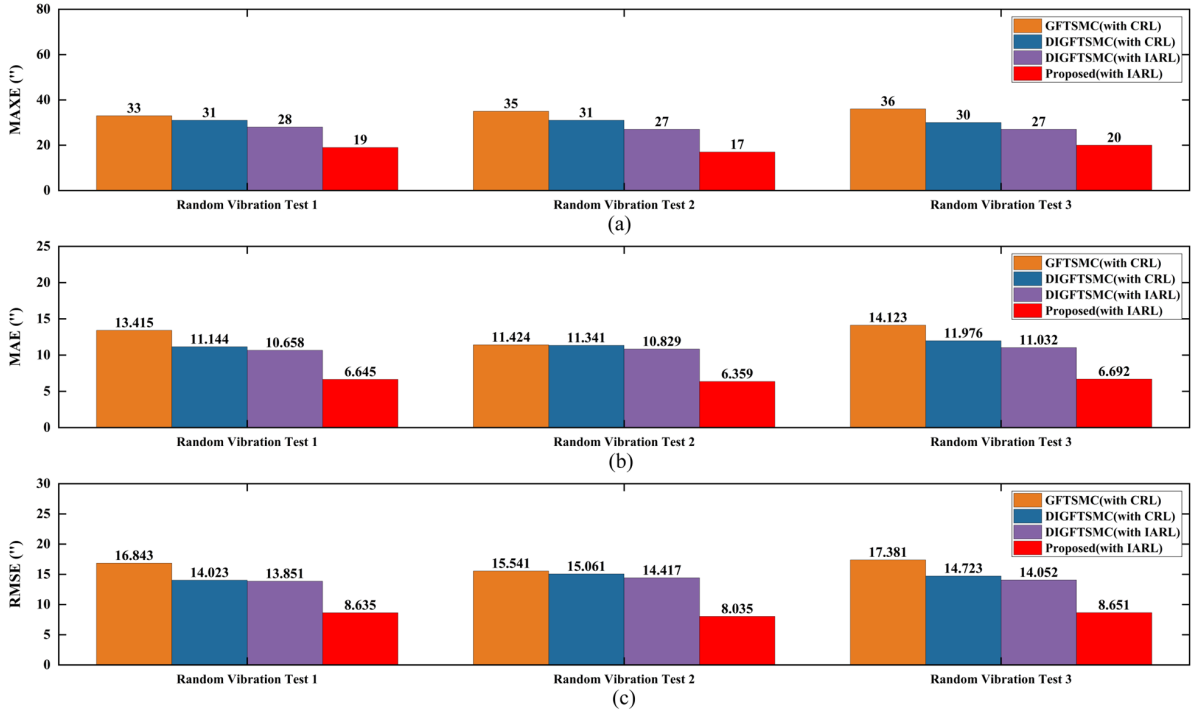


Figure 22. Quantitative analysis of three random vibration disturbance rejection tests. (**a**) MAXE. (**b**) MAE. (**c**) RMSE.

6. Conclusions

This study addresses the precision tracking challenge of voice-coil-driven FSM systems under model uncertainties and external disturbances—a critical bottleneck in high-precision optical engineering. To tackle this, we propose a refined global fast terminal sliding mode controller integrating a double-integral sliding surface, TD, LESO, and IARL. A key strength of the scheme is its synergistic module collaboration: TD generates noise-free reference differentials, LESO enables real-time disturbance estimation and suppression, double-integral terms eliminate steady-state errors, and IARL balances convergence speed with chattering suppression without excessive gains. We conducted systematic numerical simulation experiments for five control algorithms (PID controller, GFTSMC (with CRL), DIGFTSMC (with CRL), DIGFTSMC (with IARL), and the proposed controller) across four typical test scenarios, verifying the proposed controller's feasibility and performance advantages prior to physical experiments. Experimental results confirm that the proposed controller outperforms existing methods significantly: compared with the PID controller and the DIGFTSMC approach with only IARL, the step response settling time is reduced by 81.0% and 48.4%, respectively; in trajectory tracking tasks, the MAE and RMSE are decreased by 87–89% relative to the PID controller and 46–52% relative to the DIGFTSMC approach with only IARL; and in three repeated random vibration disturbance rejection, the average angular displacement fluctuation is suppressed by over 44% compared with other sliding mode control approaches. Simulation results consistently demonstrate that the proposed controller achieves faster convergence, smaller tracking errors, and stronger disturbance rejection than comparable methods, laying a solid theoretical foundation for subsequent experimental validation. A core advantage of the proposed controller is that the synergy of TD, LESO, and IARL enables a balanced optimization of tracking precision, response speed, and disturbance rejection. Notably, due to the good consistency between the simulated and experimental results, it is further established that the proposed control approach and model of FSM system are reliable. Despite these merits, limitations persist: the performance of the system relies on careful parameter tuning for specific FSM configurations, and computational complexity is manageable for the TMS320F28377D DSP, but may hinder real-time implementation in resource-constrained microcontrollers. Future work will extend the framework to multi-axis FSMs for coupled dynamics and integrate intelligent optimization algorithms for adaptive parameter tuning under complex time-varying disturbances.

Author Contributions: Conceptualization, X.J. and Q.C.; methodology, X.J., Q.C. and R.X.; software, X.J.; validation, X.J.; investigation, X.J. and Q.C.; resources, Q.C. and L.L.; writing—original draft preparation, X.J.; writing—review and editing, X.J. and Q.C.; supervision, Q.C.; funding acquisition, Q.C. All authors have read and agreed to the published version of the manuscript.

Funding: This research was supported by the National Natural Science Foundation of China (Grant No. 62475017).

Data Availability Statement: The original contributions presented in this study are included in the article. Further inquiries can be directed to the corresponding author(s).

Acknowledgments: The authors gratefully acknowledge the editors and anonymous reviewers for their insightful comments and constructive suggestions, which have greatly improved the quality of this paper.

Conflicts of Interest: The authors declare no conflicts of interest.

References

1. Kluk, D.J.; Boulet, M.T.; Trumper, D.L. A high-bandwidth, high-precision, two-axis steering mirror with moving iron actuator. *Mechatronics* **2012**, *22*, 257–270. [CrossRef]
2. Lv, T.; Ruan, P.; Jiang, K.; Jing, F. Modeling and analysis of fast steering mirror disturbance effects on the line of sight jitter for precision pointing and tracking system. *Mech. Syst. Signal Process.* **2023**, *188*, 110002. [CrossRef]
3. Weng, Z.; Xue, W.; Zhu, X.; Wang, M.; Su, Y.; Yang, Y.; Liu, Y.; Huang, H.; Wang, Y.; Xie, K.; et al. Integrated piezoresistive sensor for high-precision closed-loop control of piezoelectric MEMS fast steering mirror. *Sens. Actuators A-Phys.* **2025**, *390*, 116614. [CrossRef]
4. Fan, M.-W.; Huang, L.-H.; Li, M.; Chang-Hui, R. High-bandwidth control of piezoelectric steering mirror for suppression of laser beam jitter. *Acta Phys. Sin.* **2016**, *65*, 024209. [CrossRef]
5. Han, W.; Shao, S.; Zhang, S.; Tian, Z.; Xu, M. Design and modeling of decoupled miniature fast steering mirror with ultrahigh precision. *Mech. Syst. Signal Process.* **2022**, *167*, 108521. [CrossRef]
6. Zhang, Y.; Zhang, J.; Sun, C.; Zhou, K. System Identification and Tracking, Antidisturbance Composite Control Technology of Voice Coil Actuator Fast Steering Mirror. *IEEE Trans. Ind. Electron.* **2024**, *71*, 11146–11155. [CrossRef]
7. Gao, P.; Su, X.; Pan, Z.; Liu, R.; Zhang, W.; Cao, Y.; Wang, L. Image motion compensation control method for the dynamic scan and stare imaging system. *Appl. Opt.* **2024**, *63*, 8890–8897. [CrossRef]
8. Wang, L.; Zhang, F.; Haonan, S.; Zhao, J.; Yiran, H.; Riping, Z.; Peng, G.; Wang, C. High-dynamic tracking control technology for the fast-steering mirror in a laser communication system. *Appl. Opt.* **2025**, *64*, 8240–8247. [CrossRef]
9. Sun, J.; Ding, Y.; Zhang, H.; Yuan, G.; Zheng, Y. Conceptual Design and Image Motion Compensation Rate Analysis of Two-Axis Fast Steering Mirror for Dynamic Scan and Stare Imaging System. *Sensors* **2021**, *21*, 6441. [CrossRef]
10. Shi, K.; Yang, H.; Peng, J.; Ma, Y.; Zhang, H. High-Speed Target Location Based on Photoelectric Imaging and Laser Ranging with Fast Steering Mirror Deflection. *Photonics* **2025**, *12*, 108. [CrossRef]
11. Lahari, S.A.; Raj, A.; Soumya, S. Control of fast steering mirror for accurate beam positioning in FSO communication system. In Proceedings of the 2021 International Conference on System, Computation, Automation and Networking (ICSCAN), Puducherry, India, 30–31 July 2021; pp. 1–6.
12. Wang, Z.; Zhang, B.; Li, X.; Zhang, S. Study on application of model reference adaptive control in fast steering mirror system. *Optik* **2018**, *172*, 995–1002. [CrossRef]
13. Subaşı, Ö.; Erol, B.; Altıner, B.; Turan, H.; Baci, N. H∞ controller design for the mitigation of atmospheric effects on the laser beam pointing. *Trans. Inst. Meas. Control.* **2021**, *43*, 1786–1801. [CrossRef]
14. Dong, Q.; Liu, Y.; Zhang, Y.; Gao, S.; Chen, T. Improved ADRC with ILC Control of a CCD-Based Tracking Loop for Fast Steering Mirror System. *IEEE Photonics J.* **2018**, *10*, 6601314. [CrossRef]
15. Li, Z.; Li, L.; Zhang, J.; Feng, W. System modeling and sliding mode control of fast steering mirror for space laser communication. *Mech. Syst. Signal Process.* **2024**, *211*, 111206. [CrossRef]
16. Qin, G.; Wang, M.; Cao, G.; Wang, Q.; Liao, Y. PID Sliding Mode Control of PMSM Based on Improved Terminal Sliding Mode Reaching Law. *Energies* **2025**, *18*, 2661. [CrossRef]
17. Hu, M.; Li, J.; Li, X.; Zhao, H.; Huang, Y.; Han, J.; Gu, W.; Cheng, G. Non-singular terminal sliding mode control algorithm design based on extended state observer. *J. Mech. Sci. Technol.* **2024**, *38*, 3695–3707. [CrossRef]
18. Yang, L.; Yang, J. Nonsingular fast terminal sliding-mode control for nonlinear dynamical systems. *Int. J. Robust Nonlinear Control.* **2011**, *21*, 1865–1879. [CrossRef]
19. Jamshidi, S.; Safa, A.; Mirzajani, S. Continuous Nonsingular Fast Terminal Sliding Mode Control for a Free Gyro Stabilized Mirror System. *IEEE Trans. Autom. Sci. Eng.* **2025**, *22*, 10937–10947. [CrossRef]
20. Liu, C.; Liu, W.; Ma, H.; Xiong, Z.; Li, Y. Saturated Prescribed Space–Time Adaptive Sliding Mode Control with its Implementation on Piezo-Actuated Fast Steering Mirror. *IEEE Trans. Circuits Syst. II Express Briefs* **2024**, *71*, 1346–1350. [CrossRef]
21. Wang, L.; Wang, Z.; Wang, F.; Shi, G.; Xu, R. Robust finite-time adaptive control for high performance voice coil motor-actuated fast steering mirror. *Rev. Sci. Instrum.* **2022**, *93*, 125003. [CrossRef]
22. Xiong, J.J.; Chen, Y. RBFNN-Based Parameter Adaptive Sliding Mode Control for an Uncertain TQUAV with Time-Varying Mass. *Int. J. Robust Nonlinear Control.* **2025**, *35*, 4658–4668. [CrossRef]
23. Alattas, K.A.; Vu, M.T.; Mofid, O.; El-Sousy, F.F.M.; Alanazi, A.K.; Awrejcewicz, J.; Mobayen, S. Adaptive Nonsingular Terminal Sliding Mode Control for Performance Improvement of Perturbed Nonlinear Systems. *Mathematics* **2022**, *10*, 1064. [CrossRef]
24. Zhang, J.; Tan, C.P.; Zheng, G.; Wang, Y. On sliding mode observers for non-infinitely observable descriptor systems. *Automatica* **2023**, *147*, 110676. [CrossRef]
25. Choi, H.H. LMI-Based Nonlinear Fuzzy Observer-Controller Design for Uncertain MIMO Nonlinear Systems. *IEEE Trans. Fuzzy Syst.* **2007**, *15*, 956–971. [CrossRef]
26. Hu, S.; Qin, Y.; Yang, J. Global Fast Terminal Sliding Mode Control of Magnetic Levitation System Based on Improved Extended State Observer. *Int. J. Control. Autom. Syst.* **2025**, *23*, 1469–1483. [CrossRef]

27. Wang, X.; Li, X.; Zhang, D.; Wu, T. An improved global fast terminal high-order sliding mode control strategy based on novel reaching law for improving PMLSM dynamic performance. *Energy Rep.* **2023**, *9*, 829–838. [CrossRef]
28. Fu, F.; Lei, X.; Wang, R. A Compound Control Method Based on the Adaptive Linear Extended State Observer and Global Fast Terminal Sliding Mode Control for Inertially Stabilized Platform. *Machines* **2022**, *10*, 426. [CrossRef]
29. Lei, Y.; Xia, Y.Q.; Zhang, N. Design of a high speed stable platform control system based on improved tracking differentiator. *AIP Adv.* **2025**, *15*, 055002. [CrossRef]
30. Gao, Z. Scaling and bandwidth-parameterization based controller tuning. In Proceedings of the IEEE American Control Conference 2003, Denver, CO, USA, 4–6 June 2003; pp. 4989–4996.
31. Yu, S.; Yu, X.; Shirinzadeh, B.; Man, Z. Continuous finite-time control for robotic manipulators with terminal sliding mode. *Automatica* **2005**, *41*, 1957–1964. [CrossRef]

Disclaimer/Publisher's Note: The statements, opinions and data contained in all publications are solely those of the individual author(s) and contributor(s) and not of MDPI and/or the editor(s). MDPI and/or the editor(s) disclaim responsibility for any injury to people or property resulting from any ideas, methods, instructions or products referred to in the content.